Journal of Nuclear Materials 509 (2018) 550–565

Contents lists available at ScienceDirect

Journal of Nuclear Materials

journal homepage: www.elsevier.com/locate/jnucmat

Multilayer interface tracking model of zirconium clad oxidation

Michael Reyes [a], Asghar Aryanfar [b, c], Sun Woong Baek [a], Jaime Marian [a, c, *]

[a] Department of Mechanical and Aerospace Engineering, University of California Los Angeles, Los Angeles, CA, 90095, USA
[b] Civil, Mechanical and Energy Engineering, Bahçeşehir International University, Istanbul, Turkey
[c] Department of Materials Science and Engineering, University of California Los Angeles, Los Angeles, CA, 90095, USA

ARTICLE INFO

Article history:
Received 23 December 2017
Received in revised form
11 July 2018
Accepted 12 July 2018
Available online 18 July 2018

Keywords:
Zirconium oxide
Zircalloy clad
Zircalloy corrosion
Oxidation
Nuclear reactor

ABSTRACT

We present a numerical model to predict oxide scale growth and failure in zirconium clad exposed to water in out-of-pile conditions. The model includes the formation of two oxide sublayers on top of the metal clad, whose interfaces are tracked using a Stefan model coupled to diffusion kinetics. The kinetics is coupled to a thermal model that accounts for temperature gradient effects via thermo-migration inside the clad. The model also includes a mechanical failure criterion based on the accumulation of compressive stresses in the oxide near the interface with the metal. We present results of oxygen diffusion into the clad, oxide formation as a function of time, and oxide fragmentation by mechanical failure. We find that the growth of the oxide scale as the cubic root of time is recovered for a special charge distribution near the oxide interface. This charge distribution can be suppressed via alloying, which explains the square root scaling for certain Zr alloys. A sensitivity study has been conducted, showing that variations of ± 15% in selected model parameters result in approximately ± 5% changes in model predictions.

1. Introduction

Corrosion of metallic structural materials is an extraordinarily broad phenomenon with implications in many areas of engineering [1–3]. In nuclear reactors cores, understanding the kinetics of corrosion of metallic components is particularly challenging, due to the compounded effects of high temperature, mechanical stresses, complex coolant and fuel chemistry, and irradiation [4,5]. In light-water nuclear reactors (LWR) zirconium alloys are used as cladding materials in fuel elements to provide a mechanical barrier with a low impact on neutron economy between the coolant (water) and the fuel [6–8]. In principle, Zr clad is subjected to corrosion from the coolant (water) and fuel sides, both by way of oxygen and hydrogen penetration. The oxidation and hydriding performance of zirconium fuel components in LWRs may limit the maximum fuel discharge burn-up, which makes corrosion a critical aspect of Zr materials response in nuclear environments [9–14].

Corrosion in LWR is typically studied in autoclave experiments, subjecting components to temperatures and pressures representative of reactor operation [15–17]. These tests can be performed *in-pile*, with the autoclave directly experiencing conditions in the reactor core, or *out-of-pile*, with experiments done under controllable laboratory conditions. For obvious reasons, in-pile experiments are considered more scientifically relevant, but they are costly and slow to perform, and the different contributing factors are difficult to separate [18,19]. For their part, although out-of-pile autoclave corrosion tests developed over the years can predict some aspects of in-pile corrosion performance of zirconium alloys, these autoclave tests normally underestimate corrosion rates and do not account for irradiation effects [9,19–21]. To help bridge the gap between autoclave measurements and in-reactor Zr corrosion, several models of zirconium alloy corrosion and hydriding processes have been developed over the years [22–27]. These models focus only on certain elements of the reported observations of oxidation and hydriding, and are generally formulated 'reactively', i.e. to reproduce observed experimental time evolutions without explaining the underlying causes behind the experimental observations. This lack of predictiveness prevents these models from being used for materials evaluation and design.

The phenomenology of corrosion is such that oxidation and hydriding are typically treated separately, despite ample evidence suggesting that there exist certain synergisms between oxygen and hydrogen pickup and transport that must be considered jointly in

* Corresponding author. Department of Materials Science and Engineering, University of California Los Angeles, Los Angeles, CA, 90095, USA.
E-mail address: jmarian@ucla.edu (J. Marian).

https://doi.org/10.1016/j.jnucmat.2018.07.025
0022-3115/

corrosion of Zr [28–30]. This is partially due to the formation of a clearly distinguishable outer oxide scale and inner region where hydride platelets accumulate. In keeping with this distinction, in this paper we focus on the oxidation kinetics of Zr clad, assuming no cooperative effects from hydrogen on oxygen transport and reaction. An added challenge of considering Zr oxidation is the observation of an anomalous oxide layer thickness growth law that scales as $\sim t^{1/3}$, in contrast to the classical $\sim t^{1/2}$ scaling observed under the assumption of diffusion-limited kinetics [31–35]. There are several explanations that have been put forward to explain this anomaly, including charge imbalance [32], and hydrogen/oxygen coupling [30]. However, detailed experiments of zircalloy exposure to oxygen-only conditions have clearly revealed this cubic growth law, casting doubt on the role of hydrogen in facilitating a deviation from an ideally diffusive behavior [36–38]. Gondi and Missigoli [39] have put forward an explanation that rationalizes the cubic growth dependence based on the existence of a concentration gradient of anionic vacancies, which are generated at the oxide-metal interface and assumed to decay exponentially in space. Likhanskii and Evdokimov [28] take this line of thought further by relating the vacancy concentration gradient to differences in the Fermi level across the oxide/metal interface, which creates an electric field that is compensated by a differential vacancy concentration. Under such conditions —and when the Fermi level of metal is below that of the oxide— cubic growth develops.

As well, the zirconium oxide layer is known to lose its protective properties when it cracks catastrophically from the accumulation of compressive stresses at the oxide/metal interface. Cracking under compression can conceivably occur by either de-lamination and buckling or by shear cracking, both eventually leading to spall (fragmentation) [34]. This can also be aided by microstructural features such as grain boundaries and second-phase particles. Advanced alloys such as Zircaloy-2 and 4 and/or ZIRLO, however, are seen to reconstitute after the breakdown of the oxide layer, undergoing a renewed growth stage [13]. High temperature is also known to mitigate the breakdown of the oxide scale and above 300°C the oxide scale is expected to recover entirely. Nonetheless, the failure mechanisms of the Zr oxide layer are not yet fully understood, and a full thermo-mechanical model linking growth and failure is still lacking in the literature [8,29,40].

With the objective of shedding new light on these and other issues by using new computational and experimental understanding, in this paper, we present an comprehensive oxidation model of Zr formulated from first principles reaction kinetics and fundamental thermodynamics and mechanics. The model is parameterized using electronic structure calculations and experiments and captures both the protective oxide layer growth and runaway growth after oxide scale fragmentation. First, we describe the fundamental chemistry and phenomenology of the oxidation process followed by a mathematical formulation of the model. We then provide numerical results under a number of conditions relevant to LWR operation. We finalize with a discussion of the results and the implications of our modeling approach for zircalloy corrosion.

2. Chemical reaction kinetics model

2.1. Low-temperature Zr oxide reaction chemistry

Uniform corrosion of Zr can be considered an electrochemical process defined by the cathodic reduction of water:

$$2H_2O + 4e^- \rightarrow 2O^{2-} + 2H_2 \quad (1)$$

and an anodic oxidation step:

$$Zr + 2O^{2-} + 2V^{O}_{ZrO_2} \rightarrow ZrO_2 + 4e^- \quad (2)$$

which, when combined, leads to the standard stoichiometric reaction:

$$Zr + 2H_2O \rightarrow ZrO_2 + 2H_2 \quad (3)$$

with $V^{O}_{ZrO_2}$ denoting a structural oxygen vacancy in ZrO_2. In the above reaction, we have chosen to write the hydrogen term in terms of molecular hydrogen H_2. However, we note that a portion of that hydrogen can remain as atomic hydrogen and either stay dissolved in water or penetrate the solid clad and contribute to internal hydride formation. We will get back to this issue in Section 4. Reaction (3) represents an ideal stoichiometric reaction of stable chemical species. However, in conditions of impoverished oxygen concentration such as near the oxide/metal interface, an incomplete reaction (3) may occur, leading to the formation of non-stoichiometric ZrO_{2-x}. It is generally thought that the monoclinic α-ZrO_2 phase admits a negligible range of non-stoichiometry, undetectable by conventional techniques [41]. Conversely, metallography [42] and mass spectroscopy [43] measurements have established the concentration limit of the sub-stoichiometric tetragonal β-ZrO_{2-x} phase at $x < 0.02$. This is not a minor detail, as such small deviations, among other factors, may be behind the stabilization of tetragonal zirconia (which at ambient pressure occurs only above 1200 K, cf. refs. [41,44]) near the interface, in coexistence with the monoclinic phase. As well, nonstoichiometry may play a role in the emergence of a local charge imbalance at the oxide/metal interface, as will be discussed below.

Experimental [41] and computational [44] descriptions of the phase diagram below 1200 K agree that the first compounds that appear after the metal solid solution phase (α-Zr) are ordered ZrO_z hexagonal metallic compounds —sometimes termed 'suboxides'— with stoichiometries ranging from $z = 1/6$ to $z = 1/2$ (which are often designated by descriptors such as α''_2, α''_3, or α' [41]). After that, the experimental data are inconclusive as to the phases to be expected. However, recent density functional theory (DFT) calculations suggest that a line compound with perfect stoichiometry ZrO ($z = 1$) emerges in coexistence with the metallic α' phase ($ZrO_{1/2}$) all the way to the monoclinic zirconia phase boundary (α-ZrO_2), which starts to nucleate at 1/2 oxygen atomic fraction [44]. This phase, known as δ', forms in a distorted simple hexagonal crystal lattice akin to that of α-TiO. Recent experimental measurements in several Zr-based systems show clear evidence of the formation of this phase (as well as $ZrO_{1/2}$) behind the zirconia layer in specimens exposed to 360 °C water [45–47].

In view of this picture, and to be consistent with the most recent experimental evidence, we design our model to consist of three consecutive layers (α-ZrO_2)-(δ' - ZrO)-(α-Zr) separated by two distinct interfaces evolving in time according to chemical, thermal, and mechanical constraints. In the following, the use of the word 'oxide' is applied only to the α-ZrO_2 layer.

2.2. Qualitative picture of the structural growth of zirconia films

The oxygen ions available from the reduction of water at the clad outer surface penetrate in the Zr matrix via diffusion. Under in-pile conditions, diffusion occurs against a temperature gradient of approximately 60 K over 600 μm [48], which accelerates oxygen transport as it penetrates the clad. As the oxygen concentration builds up, the resulting Zr-O mixtures evolve through the different phases discussed above. When the ratio of O and Zr atoms reaches a value of 1:1 corresponding to the δ'-ZrO phase, a well-defined interface appears, separating the ZrO from the region containing

the metal and other suboxides[1]. As the atomic fraction of oxygen approaches 2/3, the oxide forms, resulting in a second interface separating it from the δ' phase. However, because the monoclinic ZrO_2 phase that corresponds to low temperature Zr oxide does not form under sub-stoichiometric conditions, the first oxide phase to emerge is a tetragonal β-ZrO_{2-x} phase. The tetragonal phase is believed to be stabilized at low temperatures by the compressive stresses that develop between the α-Zr matrix which opposes the transformation to the less dense monoclinic form [49,50]. In addition, the stability of the tetragonal phase can be aided by keeping the oxide particle size at less than approximately 30 nm, due to lower surface energies compared with monoclinic [51,52].

The oxide that starts to form consists of arrays of nano-crystals of ZrO_{2-x} (roughly equiaxed for in-pile conditions [31], while columnar out-of-pile [48]), with many different orientations relative to the orientation of the Zr grain on which they form. As just discussed, the internal structure of these crystallites is initially that of tetragonal zirconia [48,53], and although their crystallographic orientation is typically very difficult to establish, one should expect these crystallites to grow with orientations that minimize the stress due to the volume change on going from Zr to zirconia (the Pilling-Bedworth[2] ratio of 1.56). Recent work has indeed established that the oxide consists mainly of well-oriented columnar monoclinic grains aligned with ⟨001⟩ directions parallel to the metal/oxide interface, with sporadic tetragonal grains interspersed throughout the oxide with orientations significantly deviated from the expected ⟨001⟩ [54]. At this stage, free oxygen diffusion is thought to occur preferentially along the grain boundaries of these oxide crystallites within the ZrO_{2-x} layer, which accelerates oxygen transport with respect to bulk diffusion. Weight loss experiments show that the oxide scale thickness under these conditions grows as $t^{1/2}$ [34,48,55,56].

As the oxygen continues to penetrate the clad, the stoichiometric oxide concentration is first reached near the environment side. This prompts the oxide crystals to begin transforming into a more stable monoclinic phase. This tetragonal → monoclinic zirconia transformation is martensitic and results in the generation of microcracks —possibly compounded by residual stresses developed during the metal-to-oxide transformation[3]— in the oxide due to the volume change associated with the phase change [54,57,58]. As the oxide thickens, it transitions to a $t^{1/3}$ growth dependence (at least under PWR operating temperatures [8,13,48,53,55,59]), the mechanisms of which are not fully understood. Further oxide growth results in the eventual activation of cracks, leading to Stage 2 kinetics. Thus, at any given point, one expects a layer of tetragonal zirconium oxide to exist adjacent to the oxide/ZrO (or metal) interface where the free oxygen concentration is less than stoichiometric, whereas at the oxide/water interface these crystallites transform to monoclinic zirconia with an intrinsic distribution of cracks. We have modeled the coexistence of the two allotropes of ZrO_2 in a previous study [60]. In this work, however, we make no distinction between sub-stoichiometric tetragonal zirconia and monoclinic zirconia, which are both bundled into a single 'oxide' layer.

2.3. Kinetic model

To predict the evolution of the interfaces that define the limits of the different layers, we resort to a *Stefan* model [61]. The Stefan formulation has been widely used to solve moving boundary problems involving mass and heat transport [61–63]. In the present study, interfaces move as a consequence of oxygen flux discontinuities resulting from diffusion in different media. The geometry considered for the model is shown in Fig. 1. As the figure shows, with three distinct layers of different composition —representing, respectively, ZrO_2, ZrO, and α-Zr (and its suboxides)—, two evolution equations must be defined for the two interfaces separating each layer. The first for s_1, the ZrO_2/ZrO interface, and the second, s_2, for the ZrO/metal interface:

$$\dot{s}_1 = \frac{J_{III}}{2\rho_{Zr}} = -\frac{D_{III}}{2\rho_{Zr}}\frac{\partial c_{III}}{\partial y} \tag{4}$$

$$\dot{s}_2 = \frac{J_{II}}{\rho_{Zr}} = -\frac{D_{II}}{\rho_{Zr}}\frac{\partial c_{II}}{\partial y} \tag{5}$$

where the roman numeral I refers to the ZrO_2 layer and II to ZrO (cf. Fig. 1), J_I and J_{II} are the mass fluxes, D_I and D_{II} the oxygen diffusivities, and ρ_{Zr} is the atomic density of the metal. Determination of the fluxes requires solving a general mass balance equation of the type:

$$\frac{\partial c_i}{\partial t} = \nabla(D_i\nabla c_i) + \frac{U_i D_i}{kT^2}\nabla c_i \nabla T + \frac{q_i D_i}{kT}\nabla(c_i \nabla\phi) \tag{6}$$

also known as the *drift-diffusion* equation [64]. The *i* subindex refers to zones I, II, and III. The terms on the r.h.s. of eq. (6) are:

- The first term is standard *Fickian* diffusion in the presence of a concentration gradient.
- The second term is the so-called *thermo-migration* contribution, which depends on the temperature gradient and where *U* is the activation energy for diffusion. According to the classical theory of thermomigration (also known as *Soret-Ludwig* effect), vacancy mediated motion of substitutional atoms is expected to occur down the temperature gradient, while interstitial solutes move in the opposite direction. Experiments and calculations [65,66] have provided evidence of oxygen diffusion in α-Zr down the temperature gradient, suggesting an interstitial diffusion mechanism. According to convention, such thermomigration is labeled 'positive', and thus we show it as additive in the equation.

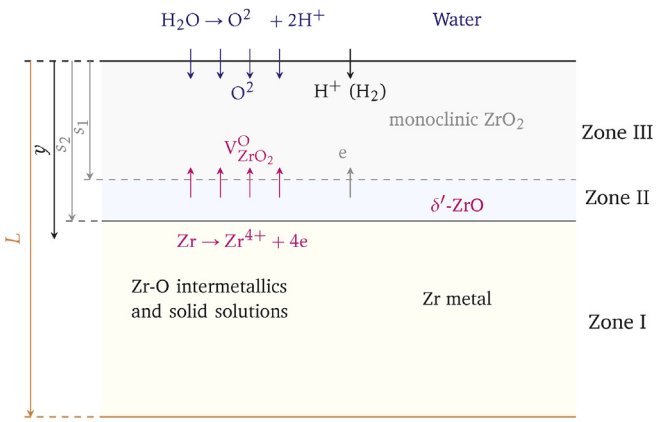

Fig. 1. Schematic diagram (not to scale) of the geometry considered in the corrosion model developed in this work. *y* is the depth variable, s_1 is the location of the ZrO_2/ZrO interface, s_2 is the location of the ZrO/metal interface, and *L* is the total thickness of the clad. The chemical processes occurring at each interface are shown for reference.

[1] Although it is not clear that this ZrO layer can be considered a barrier layer.

[2] Defined as PBR $= \frac{V_{ZrO_2}}{V_{Zr}} = \frac{\rho_{Zr}}{\rho_{ZrO_2}} = 1.56$, where *V* is the molar volume and ρ the atomic density.

[3] Not eliminated completely despite the orientation relations among zirconia crystallites alluded to above.

- The third term represents *electro-migration*, where q is the charge of the diffusing species (e.g. -1 for electrons), and ϕ is the electrical potential, which can be determined by solving Poisson's equation:

$$\nabla^2\phi = -\frac{\rho}{\varepsilon} \tag{7}$$

where ρ is the charge density and ε is the dielectric permittivity.

As discussed in Section 2.1, with the buildup of O in the metal, a series of configurations ranging from a solid solution to various subsaturated intermetallic phases begin to form. These phases effectively *immobilize* oxygen by dissolving it internally and removing it from the free oxygen concentration. The relevance of each of the terms in eq. (6) depends on the chemistry and kinetics in each layer, which we discuss next.

2.3.1. Zone I: formation of the Zr-O solid solution

As free oxygen penetrates into the clad, a Zr-O solid solution is formed. In accordance with the zirconium-oxygen phase diagram [44], at the temperatures of interest here of 600 ~ 660 K oxygen is soluble up to around 20 at.%. In the metallic layer, local charge equilibrium is assumed so that drift due to electro-migration can be neglected. However, the existing temperature gradient activates thermo-migration. The resulting equation is:

$$\frac{\partial c_{\mathrm{I}}}{\partial t} = D_{\mathrm{I}}\left(\frac{\partial^2 c_{\mathrm{I}}}{\partial y^2} + \frac{U_{\mathrm{I}}}{kT^2}\frac{\partial c_{\mathrm{I}}}{\partial y}\frac{\partial T}{\partial y}\bigg|_{\mathrm{I}}\right) \tag{8}$$

where $D_{\mathrm{I}} = D_0^{\mathrm{I}}\exp\left(-\frac{U_{\mathrm{I}}}{kT}\right)$ is the diffusivity of oxygen in α-Zr, assumed to be independent of the oxygen content.

2.3.2. Zone II: diffusional growth of the δ'-ZrO layer

At an atomic fraction of 0.5, the first line compound appears with the formation of the δ' phase. Line compounds are no longer capable of immobilizing oxygen, as they correspond to saturated phases. This results in the formation of a distinct ZrO layer with a fixed composition, clearly seen in atom probe tomography experiments as a plateau in the measured oxygen concentration at 50% [45–47]. As above, charge equilibrium is assumed so that the mass balance equation reads:

$$\frac{\partial c_{\mathrm{II}}}{\partial t} = D_{\mathrm{II}}\left(\frac{\partial^2 c_{\mathrm{II}}}{\partial y^2} + \frac{U_{\mathrm{II}}}{kT^2}\frac{\partial c_{\mathrm{II}}}{\partial y}\frac{\partial T}{\partial y}\bigg|_{\mathrm{II}}\right) \tag{9}$$

where D_{II} is the diffusivity of oxygen in ZrO.

2.3.3. Zone III: growth of the oxide scale

As in zone II, the growth of zone III, referred to as *oxide scale* hereafter, is driven by an oxygen flux imbalance at the ZrO/ZrO_2 interface. However, for completeness of the model, it is necessary to account for the electric field created by charged species gradients, including oxygen anions and electrons. Therefore, the complete equation is used for this layer:

$$\frac{\partial c_{\mathrm{III}}}{\partial t} = D_{\mathrm{III}}\left[\frac{\partial^2 c_{\mathrm{III}}}{\partial y^2} + \frac{U_{\mathrm{III}}}{kT^2}\frac{\partial c_{\mathrm{III}}}{\partial y}\frac{\partial T}{\partial y}\bigg|_{\mathrm{III}} + \frac{q}{kT}\left(\frac{\partial c_{\mathrm{III}}}{\partial y}\frac{\partial \phi}{\partial y} + c_{\mathrm{III}}\frac{\partial^2\phi}{\partial y^2}\right)\right] \tag{10}$$

where D_{III} is the oxygen diffusivity in the oxide.

As Couet et al. [67] have discussed, the existence of an oxygen concentration gradient across the oxide layer has not been firmly established experimentally, although several studies make use of this concept to explain non-parabolic growth in corroded Zr [28,68]. Couet et al. have developed kinetic models that ensure charge balance between the anionic and cationic mass flows giving rise to zero charge current condition [67]. Here, in the spirit of the results by Beie et al. [69], who measured the voltage difference between the metal and the oxide surfaces in non-stoichiometric $ZrO_{2\text{-}x}$, we adopt a simpler approach by using a fast-decaying charge density distribution concentrated near the interface with the ZrO layer:

$$\rho(y) = \rho_0\exp\left(-\frac{s_1 - y}{\lambda}\right) \tag{11}$$

where ρ_0 is that charge density at the interface and λ is a spatial constant. We reiterate that the justification for using this expression for the charge density lies in the existence of a thin layer of $ZrO_{2\text{-}x}$ where non-stoichiometry and high compressive stresses can result in extra oxygen vacancies that can trap electrons and create a charge gradient, as has been discussed by Bell et al. [70,71]. From a numerical point of view, expression (11) is straightforward to integrate, which allows as to write the electrical potential and its first derivative as:

$$\phi(y) = -\frac{\lambda^2\rho(y)}{\varepsilon}, \nabla\phi(y) = -\frac{\lambda\rho(y)}{\varepsilon}$$

During Stage 1 growth, equations (8)–(10) can be solved in one dimension (y) using the finite difference model subjected to the following dynamic boundary conditions:

$$c_{\mathrm{I}}(y,0) = 0, y > s_2$$
$$c_{\mathrm{I}}(s_2,t) = c_{\mathrm{II}}(s_2,t) + \rho_{\mathrm{Zr}}$$
$$c_{\mathrm{II}}(s_1,t) = c_{\mathrm{III}}(s_1,t) + 2\rho_{\mathrm{Zr}}$$
$$c_{\mathrm{III}}(0,t) = C_0$$
$$\frac{\partial c_{\mathrm{I}}(L,t)}{\partial y} = 0$$

where C_0 is the (constant) oxygen concentration available at the outer clad surface. The first condition trivially states that the oxygen content in the clad at the beginning of time is zero. The next two ensure the continuity of oxygen concentration at the interfaces while the third fixes the oxygen concentration in the environment to a value set by the water chemistry, temperature, pressure, etc. Finally, the last one simply reflects the fact that no free oxygen can escape the clad into the fuel side, *i.e.* $J_{\mathrm{I}}(L,t) = 0$, where J_{I} is the free oxygen flux in the metal.

As the oxidation process continues, microcracks developed in the oxide scale created by the volume differential with respect to the Zr metal start to grow. The transformation of the tetragonal phase into the monoclinic one results in an additional expansion of ~ 3% at 0 K, as given by their respective specific volumes of 0.139 and 0.143 nm^3 [4]. Eventually, these in-grown cracks form a network, which ultimately results in fragmentation of the oxide scale, giving rise to Stage 2 growth.

2.4. Stage 2: breakaway growth of the ZrO_2 layer

Our critical assumption for Stage 2 growth is that free oxygen from the environment side becomes immediately available on the ZrO_2/ZrO interface (at $y = s_1$) via transport through the microcrack network. At the point of spall, it is assumed that the entire oxide

[4] $V_{\mathrm{t}} = a_{\mathrm{t}}^2 c_{\mathrm{t}}$; $V_{\mathrm{m}} = a_{\mathrm{m}} b_{\mathrm{m}} c_{\mathrm{m}} \sin\beta$, with $a_{\mathrm{t}} = 0.514$ nm, $c_{\mathrm{t}} = 0.526$ nm, and $a_{\mathrm{m}} = 0.518$ nm, $b_{\mathrm{m}} = 0.521$ nm, $c_{\mathrm{m}} = 0.537$ nm, and $\beta = 98.8°$ [72].

layer has become monoclinic, and the mass balance system of equations is solved again for the metal phase replacing the boundary condition for the oxygen concentration in the oxide metal interface with $c_{II}(s_1, t) = C_0$. As the oxide layer thickness increases during Stage 2, it is assumed that the cracks grow while maintaining the concentration of oxygen fixed at C_0 at the interface. This availability of free oxygen accelerates oxide layer growth, leading to breakaway behavior.

In terms of the model, the drift-diffusion equation need not be solved any longer for Zone III. Instead, only eqs. (9) and (10) need be considered with the updated *dynamic* boundary conditions:

$$c_{II}(s_1, t > t_{1\to 2}) = C_0$$

where $t_{1\to 2}$ is the time at which transition into Stage 2 occurs. Equation (4) then becomes:

$$\dot{s}_1 = \frac{C_0 v}{2\rho_{Zr}} \tag{12}$$

where v is the velocity of the viscous flow of water through the crack network. Again, we note that this is the model assumed for pure Zr, which is known to break down at less than two microns in thickness. This does not appear to be the case, however, for the oxide scale in more advanced Zr alloys, which is seen to reconstitute cyclically.

2.5. Calculating the temperature gradients

As eqs. (8)–(10) show, $T(y)$ and $\frac{dT}{dy}$ are essential inputs to the kinetic model. Calculation of the temperature gradients requires that the temperature field be defined at every (y, t) point of the finite difference mesh. For this, it is assumed that under steady state reactor operation, the heat flux flowing from the fuel side through the clad out to the coolant side is constant. The heat flux q_0 can be obtained from Fourier's law at $t = 0$ assuming a linear temperature gradient in one dimension:

$$q_0 = -\kappa_I \frac{dT}{dy} = \kappa_I \frac{T_c^0 - T_L^0}{L} \tag{13}$$

where κ_i is the thermal conductivity of the Zr metal (zone I), and T_L^0 and T_c^0 are the initial temperatures at the inner and outer positions of the clad, respectively. Further, it is assumed that T_c is constant in time (set by the coolant temperature), while the inner temperature T_L is allowed to vary as the cladding oxidizes and the overall thermal conductivity changes. As the oxide and suboxide layers build up, the temperature gradients in each one can be obtained from the following conservation law:

$$q_0 = \kappa_I \frac{T_L - T_2}{L - s_2} = \kappa_{II} \frac{T_2 - T_1}{s_2 - s_1} = \kappa_{III} \frac{T_1 - T_c^0}{s_1} \tag{14}$$

where κ_{II} and κ_{III} are the thermal conductivities of ZrO and ZrO_2, and T_1 and T_2 are the temperature at the ZrO_2/ZrO (s_1) and ZrO/Zr (s_2) interfaces, respectively. Combining eqs. (13) and (14):

$$T_1 = T_c^0 + \frac{q_0 s_1}{\kappa_{III}} \tag{15}$$

$$T_2 = T_1 + \frac{q_0 (s_2 - s_1)}{\kappa_{II}} \tag{16}$$

$$T_L = T_2 + \frac{q_0 (L - s_2)}{\kappa_I} \tag{17}$$

from which all thermal gradients can be calculated as a function of time by updating the temperature field via the thickness variables $s_1(t)$ and $s_2(t)$. Equations (15) and (16) show that the interface temperatures T_1 and T_2 are proportional to the thickness of the corresponding layers, while T_L is expected to rise as s_2 grows and the second term on the r.h.s. of eq. (17) becomes increasingly smaller.

2.6. Determining the transition time from Stage 1 to Stage 2

2.6.1. Stress buildup

The two main sources of stress during the growth of the oxide layer are thermal and growth stresses. Thermal stresses develop from differential thermal expansion between the oxide and metal layers. Assuming a biaxial stress state[5], when the oxide phase can be considered much thinner than the metallic substrate, the (compressive) hoop stress in the oxide scale is:

$$\sigma_\theta^{th} = \frac{E_{ox}}{1 - \nu_{ox}} \int_{T_s}^{T_w} \Delta\alpha(T) dT \tag{18}$$

where E_{ox} and ν_{ox} are, respectively, the Young's modulus the Poisson ratio of the oxide. $\Delta\alpha(T)$ is the differential thermal expansion:

$$\Delta\alpha(T) = \alpha_{ox}(T) - \alpha_m(T)$$

The sign of the thermal stresses depends on the conditions in the oxide scale. The thermal expansion coefficient is in most cases much higher for metals than it is for oxides. For nominal conditions, when the metal substrate is subjected to higher temperatures than the oxide scale, the metal expands by an amount that cannot be matched by the oxide scale at the oxide/metal interface. This would result in local tensile stresses on the oxide layer.

Compressive thermal stresses can appear upon cooling to room temperature of the clad, and can be responsible for oxide scale failure. However, under operating conditions, the main (and second) source of stresses are *growth* stresses due to internal oxidation. Growth stresses are mostly in-plane compressive, and they might reach important levels (up to few GPa [27,56,73]). To calculate their magnitude, we follow the ideas of Birks et al. [33]. If the oxide scale at the metal/oxide interface grows by consumption of the metallic substrate, the change of specific volume between the consumed phase and the created one would engender a volume eigenstrain (inelastic strain). The parameter associated with this phenomenon is the Pilling-Bedworth ratio (PBR, introduced above). If oxidation proceeds isotropically, the tangential strain due to oxide growth is approximately:

$$\varepsilon_{ox}^g = \frac{1}{3}(PBR - 1)$$

The stress state due to this strain is compressive and bi-axial:

$$\sigma_\theta^g = -\frac{E_{ox}}{3(1 - \nu_{ox})} \varepsilon_{ox}^g = -\frac{E_{ox}(PBR - 1)}{3(1 - \nu_{ox})} \tag{19}$$

These stresses develop mainly at the oxide/metal interface during the initial stages of oxide formation. Subsequent oxide scale

[5] The hoop stress is equal to the axial stress, $\sigma_\theta = \sigma_z$ (cylindrical coordinates).

growth is usually considered to occur without significant stress generation or deformation, as the new oxide formed can be accommodated on top of the existing layer. Thus, growth stresses maintain the oxide near the interface under compression by a constant amount independent of the oxide scale thickness. We note however that in reality oxide growth is highly anisotropic [54] and thus the above assumptions result in an overestimation of the stresses as given by eq. (19).

Next, we provide a criterion to establish under which conditions the growth of the oxide layer leads to uniform fragmentation and the loss of the protective layer.

2.6.2. Failure criterion

For compressive stresses there are two routes for spalling. The first one, involves the nucleation and growth of a wedge crack, and occurs preferentially for strong interfaces and weak oxide scales; the second is by buckling, which is preferred for weak interfaces and strong oxide scales.

Protective oxide layers display brittle characteristics at low temperatures. Hence, in the temperature range of interest for LWR operation one can apply Griffith's theory to calculate $t_{1\to 2}$. A flaw that develops in the oxide layer will continue to grow under a stress σ_{ox} if its strain energy release G exceeds the critical energy release rate G^* of the oxide [33,74]:

$$G_{ox} > G^*$$

where $G = K^2/E_{ox}$, and K is the stress intensity factor:

$$K = Y\sigma_\theta\sqrt{\pi a}$$

where a is the flaw size and Y is a geometric parameter whose value is close to unity for a small crack embedded in a two-dimensional solid. G^* can be equated to a surface energy γ, which results in the following criteria for fracture:

$$\frac{\sigma_\theta^2 Y^2 \pi a}{E_{ox}} > \gamma \tag{20}$$

This equation simply states that cracks will open creating more exposed surface when the accumulated elastic energy surpasses the surface energy. The flaw size a is not generally known, but it is typically assumed that it increases with oxide scale thickness [75]:

$$a = \varepsilon s_1$$

where ε is a proportionality constant[6]. It must be noted that eq. (20) applies to mode I crack growth under tensile stresses, which is not the case here. Instead, crack growth is more likely to occur by vacancy aggregation under compressive stresses, possibly in the manner of creep rupture (e.g. Ref. [76]). However, here we simply assume that the crack grows by the pertinent mechanism, eventually leading to fragmentation across the oxide scale. Cracks can originate at the interface of the oxide with the δ' phase, or during the tetragonal/monoclinic conversion. This can be impacted by the presence of impurities, precipitates, pores, or other cavities.

From eqs. (18) and (19), one can see that thermal stresses scale as $\sim 10^{-5}E_{ox}$, whereas growth stresses do as $\sim 10^{-1}E_{ox}$. Consequently, we only consider growth stresses for σ_{ox} in our model going forward. The failure criterion is obtained after inserting eq. (19) into eq. (20):

$$\frac{E_{ox}(\mathrm{PBR}-1)^2 Y^2 \pi \varepsilon s_1}{9(1-\nu_{ox})^2} > \gamma \tag{21}$$

The finalized criterion in usable form furnishes the critical oxide scale thickness s^* at the onset of fragmentation:

$$s^* > \frac{9\gamma(1-\nu_{ox}^2)}{E_{ox}(\mathrm{PRB}-1)^2 Y^2 \pi \varepsilon} \tag{22}$$

In this work we use eq. (22) to extract the value of ε assuming the lower end of the commonly cited values between one and two microns for s^* [21,77–79]. For the parameters listed in Table 1, ta value of $\varepsilon \approx 10^{-4}$ is obtained, suggestig that fragmentation in ZrO_2 can be triggered by very small cracks. For its part, the time $t_{1\to 2}$ is directly obtained from the $s_1(t)$ relation as $s_1(t_{1\to 2}) = s^*$.

2.7. Numerical solution procedure

Solution of the above system of coupled PDEs by the finite difference method requires that eqs. (8)–(10) be discretized in space and time. Here, we partition time and space into finite grids as follows:

$$t^i = i\delta t, j = 0, 1, 2, \ldots, N$$

and

$$y_j = j\delta y, i = 0, 1, \ldots, M$$

where the conventional notation of using superscripts to represent time (t^i) and subscripts to represent space (y_j) has been used. For uniform grids, δt and δy are simply:

$$\delta t = t/N$$

and

$$\delta y = L/M$$

with N and M representing the size of the grid, and t is the total simulated time.

Adopting a scheme where time derivatives are replaced by forward differences, and space derivatives by central differences (known as 'FTCS' scheme), the discretized form of the drift-diffusion equation for the most general case, represented by eq. (10) (Zone iii) reads:

$$\begin{aligned}\frac{c_j^{i+1}-c_j^i}{\delta t} = D_{\mathrm{III}}(T_j)\Bigg\{&\frac{c_{j+1}^i - 2c_j^i + c_{j-1}^i}{\delta y^2} + \frac{U_{\mathrm{III}}}{kT_j^2}\left(\frac{dT}{dy}\right)_{\mathrm{III}}^i \frac{c_{j+1}^i - c_{j-1}^i}{2\delta y} \\ &+ \frac{q\lambda\rho_0}{2kT_j\varepsilon\delta y}\left[\exp\left(-\frac{s_1^i - y_j^i}{\lambda}\right)\left(c_{j+1}^i - \frac{2\delta y}{\lambda}c_j^i - c_{j-1}^i\right)\right. \\ &\left. - c_{j+1}^i + c_{j-1}^i\right]\Bigg\}\end{aligned} \tag{23}$$

which can be written in explicit form as:

$$\begin{aligned}c_j^{i+1} = c_{j+1}^i(1 + a_1 + a_2 + a_3 + a_4) + c_j^i(1 - 2a_1 + a_5) + c_{j-1}^i(1 \\ + a_1 + a_2 + a_3 + a_4)\end{aligned} \tag{24}$$

with

[6] Not known for zirconia. Some works mention a value of 0.2 for iron oxide [75].

Table 1
Physical parameters used in the model. The sources for each parameter are given in Section 2.8.

Property	Symbol	α-Zr (Zone I)	ZrO (Zone II)	ZrO_2 (Zone III)
Diffusivity prefactor [m s^{-1}]	D_0	6.61×10^{-6}	1.26×10^{-11}	9.00×10^{-8}
Activation energy [eV]	U	1.9	1.24	1.24
Thermal conductivity [W m^{-2} K^{-1}]	κ	$8.8527 + 7.0820 \times 10^{-3}T + 2.5329 \times 10^{-6}T^2 + 2.9918 \times 10^{3}T^{-1}$	$\frac{\kappa_I + \kappa_{III}}{2}$	$1700T^{-1}$**
Charge Density [C m^{-2}]	ρ_0	N/A		662.0
Charge [C]	q_i	N/A		-3.20×10^{-19}
Permittivity constant [$C^2 \cdot eV^{-1}$]	ε	N/A		3.26×10^{-29}
Young's modulus [GPa]	E	N/A		236
Poisson ratio	ν	N/A		0.25
Surface energy [J m^{-2}]	γ	N/A		1.2

**With a factor of 0.86 applied if during Stage 2.

$$a_1 = \frac{D_{III}\delta t}{\delta y^2}, a_2 = a_1 \frac{U_{III}\delta y}{2kT^2}\left(\frac{dT}{dy}\right)_{III}, a_3 = -a_1 \frac{q\lambda\rho_0\delta y}{2kT\varepsilon}, a_4 = -a_3 \exp\left(-\frac{s_1 - y}{\lambda}\right), a_5 = a_3 \frac{2\delta y}{\lambda}$$

where T, y, s_1, and s_2 are all evaluated at time i and location j. The numerical stability of the explicit FTCS scheme can be assessed by means of a Neumann's analysis, which, for a purely parabolic problem is simply:

$$a_1 \leqslant \frac{1}{2}$$

This can be used as guidance when $a_1 > a_2, a_3$. For the general case given by eq. (24), we derive in Appendix B the stability criterion including all the terms given in the equation:

$$\delta t \leqslant \frac{2kT}{D_{III}\left(\frac{U_{III}}{T}\left(\frac{\partial T}{\partial y}\right)_{III} + \frac{q\lambda(\rho(y)-\rho_0)}{\varepsilon}\right)}\delta y$$

For the explicit form of eqs. (8) and (9), we simply make $a_3 = a_4 = a_5 = 0$ and replace D_{III}, U_{III}, and $(dT/dy)_{III}$ with their respective counterparts for Zones I and II in eq. (24).

The discrete update steps for s_1 and s_2 (eq. (4) and (5)) for Stage 1 growth are:

$$s_1^{j+1} = s_1^j + \frac{D_{III}\left(T_{M-1}^j\right)c_{III}^j|_{M-1}\delta t}{2\rho_{Zr}\delta y} \quad (25)$$

$$s_2^{j+1} = s_2^j + \frac{D_{II}\left(T_{M-1}^j\right)c_{II}^j|_{M-1}\delta t}{\rho_{Zr}\delta y} \quad (26)$$

where the index $(M-1)$ indicates the spatial point immediately before the corresponding interface. A schematic flow diagram of the integrated numerical model employed here is given in Fig. 2.

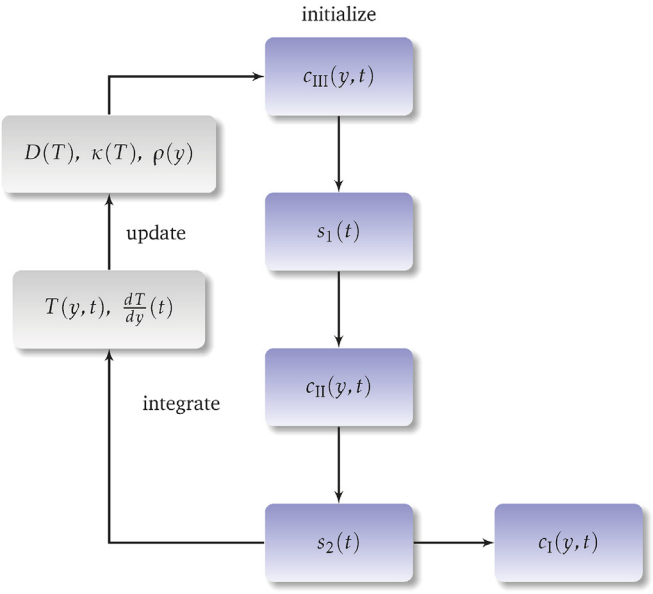

Fig. 2. Flow diagram of the numerical procedure employed here.

2.8. Model parameterization

The parameterization of the above kinetic model is an essential step in assuring the physical fidelity of the calculations. In terms of Stages 1 and 2, the key parameters are the diffusivities of free oxygen in metallic Zr, in the δ' suboxide, and in monoclinic zirconia, as well as thermal conductivities and elastic properties. A comprehensive data set satisfying the model needs is lacking, however, and here we draw from available experimental as well as numerical sources. First-principles electronic structure calculations have recently reached levels of accuracy and computational efficiency capable of providing diffusion coefficients in oxide structures. However, despite the potential of *ab initio* methods, it remains exceedingly difficult to perform calculations where the parametric space is greater than one. For this reason we complement electronic structure calculations with experimental data where needed. A compilation of all parameters used here is given in Table 1. The specific values and source of origin for each type of parameter is discussed in the following subsections.

2.8.1. Oxygen diffusivity in α-Zr

In principle, the diffusion coefficient of oxygen in hcp Zr depends both on T and z. As noted above, the temperature dependence is intrinsically captured in the Arrhenius expression. However, the dependence on z has not been established to our knowledge and thus we resort to experimental measurements where the oxygen concentration is intrinsically captured in the final value of the parameters.

Since the first experimental measurements by Pemsler [80], several studies have focused on oxygen diffusion in Zr. Ritchie and Atrens [81] have provided an excellent compilation of all the experimental data up to 1977. For temperatures in the range 290–650 °C, they give following expression:

$$D_i(T) = 6.61 \times 10^{-6} \exp\left(-\frac{1.9}{k_B T}\right) \left[\mathrm{m^2 \cdot s^{-1}}\right]$$

as the best fit to all the data. Here the activation energy is given in units of eV (per atom, equivalent to 44,000 cal per mole). Diffusion in this case is associated with jumps of oxygen interstitials in the basal plane. Above 400 °C they note that some authors have measured a different expression that yields higher diffusivities, attributable to diffusion along grain boundaries [82]:

$$D_i^{GB}(T) = 1.55 \times 10^{-10} \exp\left(-\frac{1.0}{k_B T}\right) \left[\mathrm{m^2 \cdot s^{-1}}\right]$$

Subsequent experiments have attempted to revise the measurements provided by Ritchie and Atrens, with similar values obtained [83].

The various values for U_i measured experimentally are consistent with recent density functional theory calculations of interstitial oxygen migration, where migration energies of approximately 1.0 eV are reported [66] (albeit with a relatively high degree of anisotropy depending on the nature of the jump).

2.8.2. Oxygen diffusivity in monoclinic ZrO_2

Measurements of oxygen diffusivity in monoclinic zirconia date back to the late 1960s, with the early work of Smeltzer and collaborators at high temperatures (> 1000 °C) [84,85]. A representative diffusion coefficient extracted from their data is $D_{III}(T) = 9.73 \times 10^{-7} \exp\left(-\frac{2.42}{k_B T}\right)$, while Keneshea and Douglass [86] find $D_{III}(T) = 2.34 \times 10^{-6} \exp\left(-\frac{1.96}{k_B T}\right)$, both in [$m^2$ s^{-1}] when the energies are given in eV. It appears that the measured diffusivities are relatively "fast", indicating oxygen diffusion pathways through dislocations and/or grain boundaries. As noted by Cox and Pemsler [87], however, lattice diffusion takes place with a significantly lower activation energy, <1.5 eV, which makes lattice diffusion as important as defect-mediated diffusion at temperatures below 600 °C. This is possibly due to a reduced vacancy formation energy in the presence of impurities. Cox and Pemsler's measurements, however, were made in the 400–585 °C temperature range, while the earlier work by Smith was done in the 380–386 °C [82] and also shows a reduced activation energy (1.24 eV). For this reason, in this work, we use Smith's diffusivities as given by the expression:

$$D_{III}(T) = 9.00 \times 10^{-8} \exp\left(-\frac{1.24}{k_B T}\right) \left[\mathrm{m^2 \cdot s^{-1}}\right]$$

2.8.3. Oxygen diffusivity in ZrO

The δ' suboxide is a relatively new phase and we currently do not have any sources of data for oxygen diffusivity in ZrO. Because ZrO is a saturated line compound, we assume that diffusion proceeds by way of a vacancy mechanism, and hence it is quite slow. Our approach here is to estimate the diffusivity of oxygen by matching the thickness of the ZrO layer (equal to $(s_2 - s_1)$ in our model) to experimentally-measured values, which range between approximately 60 and 120 nm [45–47]. Matching D_{II} in eq. (9) to yield a thickness of 65 nm results in a value of $D_{II} = 1.46 \times 10^{-22}$ $\mathrm{m^2 \cdot s^{-1}}$ at 600 K, which is the number used here. The reason why the oxygen diffusivity in the ZrO layer is so low is unknown to us at this point. It is known that for strong line compounds, with a very small concentration of oxygen vacancies, anion diffusion can be exceedingly low. This is a clear gap in our physical understanding of the Zr-O system, and little more than speculating can be done at this point until reliable atomistic calculations are performed to study and quantify the diffusion mechanism of oxygen in this δ' phase.

2.8.4. Thermal conductivities

Fink and Leibowitz [88] have proposed a correlation for the thermal conductivity of Zr based on a statistical analysis of experimental measurements from 1951 to 1995. The recommended equation for κ_I the thermal conductivity of zirconium in units of [W $m^{-1}K^{-1}$] from 298 through 2000 K is:

$$\kappa_I = 8.8527 + 7.0820 \times 10^{-3} T + 2.5329 \times 10^{-6} T^2 + 2.9918 \times 10^{3} T^{-1}$$

For its part, ZrO_2 is an excellent insulator and displays very low values of κ_{III}. Most of the experimental measurements, however, have been done at high temperatures in yttria or calcia-stabilized zirconia. According to Klemens [89], the temperature dependence of the thermal conductivity is well described by:

$$\kappa_{III}(T) \approx 1700 T^{-1} \left[\mathrm{W \cdot m^{-1} \cdot K^{-1}}\right]$$

During Stage 1, however, as the oxide layer grows and develops an intrinsic pore network, the thermal conductivity gradually deteriorates from its fully-dense value given by the above expression. To reflect this, we use the corrections to κ_{III} developed by Nait-Ali et al. [90] for porous zirconia:

$$\kappa_{III}(T, f) = \kappa_{III}(T)\left(1 - \frac{3f}{2+f}\right) \tag{27}$$

where f is the pore volume fraction. Further, assuming values of $f \approx 0.14$ during the onset of spall [91], we adopt a linear time dependence for f between $t = 0$ and $t = t_{1\to 2}$ from zero to its maximum value of 0.14. Once the oxide layer fails, the coolant permeates through the pores and equalizes the temperature across the entire layer.

As above, we do not know of any data for the thermal conductivity in ZrO, and as a first-order approximation, here we simply take κ_{II} as the average between κ_I and κ_{III}.

2.8.5. Electrical properties

The constants involved with the electro-migration terms in eq. (6) are the charge of oxygen anions, q_i, the charge density at the oxide interface, ρ_0, the absolute permittivity of ZrO_2, ε, and the decay constant, λ. We use a value of $\varepsilon = 3.26 \times 10^{-29}$ C^2 eV^{-1} from various measurements [92,93]. The charge of O^{2-} is simply $q_i = -3.20 \times 10^{-19}$ C, while ρ_0 is used as a fitting parameter. We find a value of $\rho_0 = 662.0$ $\mathrm{C \cdot m^{-2}}$ satisfactory for pure Zr under the conditions studied here. It is difficult to assess whether this is a reasonable number due to a lack of dedicated measurements in nuclear-grade Zr, although it is larger than measurements of charge densities at oxide interfaces in metal/semiconductor junctions involving Zr [94,95]. Finally, we just make $\lambda = dy$.

2.8.6. Mechanical properties

Very little work is reported in literature on the elastic properties of pure monoclinic zirconia. Elastic constants have been derived by several authors using lattice vibration models for tetragonal zirconia [96]. In monoclinic single crystals, Chan et al. [97] have done measurements up to 1000 °C using ultrasonic velocity measurements by Brillouin scattering. Yeugo et al. [98] have compiled the different values published in the literature and report a value of $E_{ox} = 236$ GPa between 300 and 600 °C for monoclinic zirconia. This is what is used in eqs. (18)–(22) above.

Table 2
Numerical parameters used in the model.

L [μm]	T_0 [K]	T_L^0 [K]	C_0 [m^{-3}]	ρ_{Zr} [m^{-3}]	s^* [μm]	δt [h]	δy [μm]	λ
600	600	660	1.56×10^{28}	4.31×10^{28}	1.27	0.011	0.058	δy

For Poisson's ratio we simply use a value of $\nu_{ox} = 0.25$ as given in commercial databases [99], while the surface energy of monoclinic zirconia has been measured at $\gamma \approx 1.2$ J m^{-2} [52,100]. Equation (22) can then be used to estimate either s^* or ε from knowledge of one or the other.

2.9. Physical dimensions and boundary conditions

The final set of parameters needed to run the model defines the physical dimensions and boundary conditions of the model. The clad thickness L, and the inner and outer clad temperatures T_0 and T_L (at $t = 0$) are nominal values in LWR.

The value of C_0 can vary among several LWR concepts, as the oxygen partial pressure in water depends on temperature, pressure, and water chemistry. Values for pressurized water reactors (PWR), boiling water reactors (BWR), water-water energetic reactors (VVER), and heavy water CANDU reactors are provided by Billot et al. [101]. However, in general, the amount of oxygen (and hydrogen) dissolved in water is relatively small in the temperature range explored here, and oxygen ions are made available by the reduction of water on the surface of the clad. For example, the value reported by Pemsler in his studies of water corrosion of Zr is of 0.54 g·cm^{-3} (or 1.69×10^{28} m^{-3}) [80]. Here we fit the value of C_0 such that the model predicts a Stage 1→2 transition of 55 days[7] consistent with the measurements by Motta et al. [45,102]. All these numbers are given in Table 2.

As well, for consistency with experiments, we have decided to use a constant value of $s^* = 1.27$ μm [21], regardless of reactor type. From eq. (22), this choice results in a value of $\varepsilon \approx 4\times10^{-6}$, much smaller than the value reported for other oxides [75]. Finally, the spatial and temporal mesh sizes, δy and δt are also given in the Table.

3. Results

As explained in Section 2.3, our model provides a spatio-temporal picture of the oxidation process in Stages 1 and 2. Next, we present our main results and a brief discussion about their relevance and validity.

3.1. Pure Zr

We begin with the evolution of the inner clad temperature, T_L, with time. Fig. 3 shows the variation of T_L with exposure time. As the figure shows, the variation is of only two degrees, which has a negligible impact on the temperature gradients that develop in each of the layers captured by the model. We emphasize that the total heat flux is conserved (as to mimic constant power conditions in a LWR), and T_L changes as a consequence of keeping the coolant temperature fixed at 600 K.

Fig. 4 shows the temperature profiles at 0, 20, and 60 days, calculated according to eqs. (15)–(17). After 55 days (breakaway oxidation), the temperature in the entire oxide layer equalizes with the coolant temperature due to water percolation through the crack network. Although the absolute temperature changes are small,

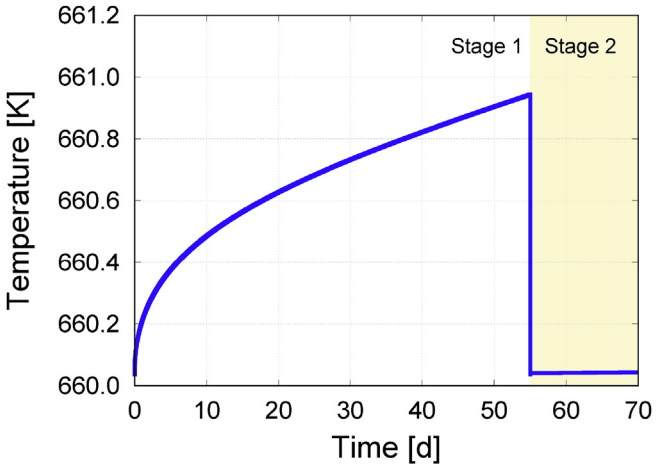

Fig. 3. Variation of the temperature at $y = L$ (inner clad radius, fuel side) with exposure time. The temperature rises steadily during Stage 1 and then drops quickly after the failure of the oxide layer.

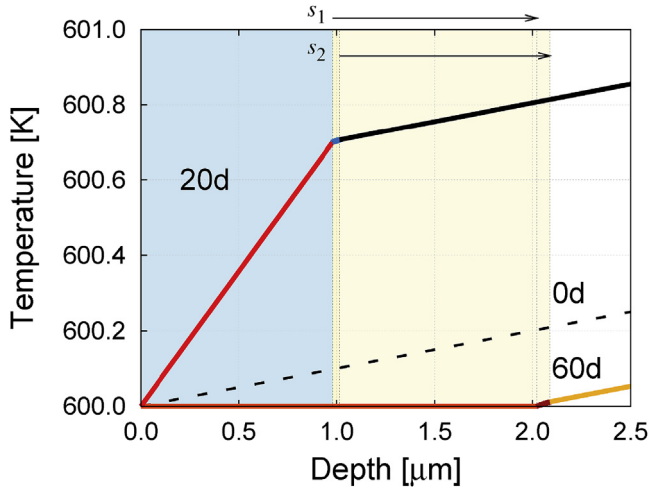

Fig. 4. Temperature depth profiles at 0, 20, and 60 days. The graph shows the growth of the oxide layer(s) during each time interval. Also shown is the flat temperature profile.

gradients on the order of 10^6 K m^{-1} are seen to develop in the oxide scale, which is what is important for thermomigration. After breakaway, the absence of such gradients in the ZrO_2 layer implies no effect on oxygen diffusion.

Next, we study the oxygen penetration inside the clad as a function of time. Fig. 5 shows the total oxygen concentration as a function of depth for two distinct time instants in Stage 1. These profiles result from solving the drift-diffusion equation (cf. eq. (8) through (10)) in each one of the three zones depicted in Fig. 1. Solid and dashed lines correspond to the oxygen concentration profile at 20 and 40 days of exposure, respectively. As the figure shows, mass continuity exists at the interfaces, marked by the dashed lines in each case. However, the profiles clearly show discontinuities in the mass fluxes, which results in net interface

[7] For pure Zr specimens.

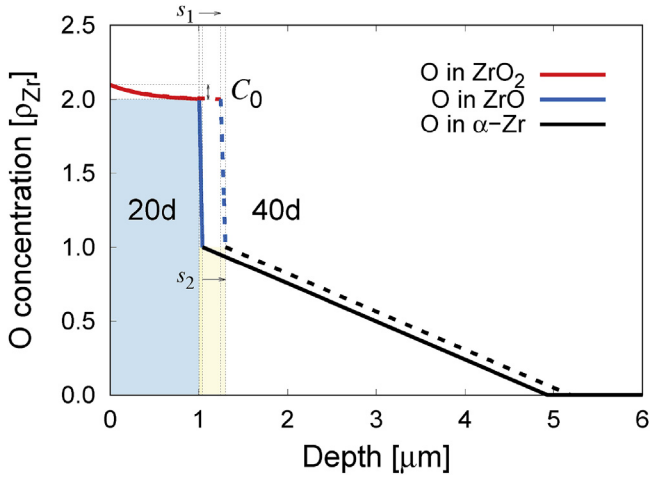

Fig. 5. Depth profile of the total oxygen concentration at two instants during oxide scale growth. The concentration is expressed as in units of ρ_{Zr}. The shaded areas in the graph represent the thickness of the ZrO_2 and ZrO layers.

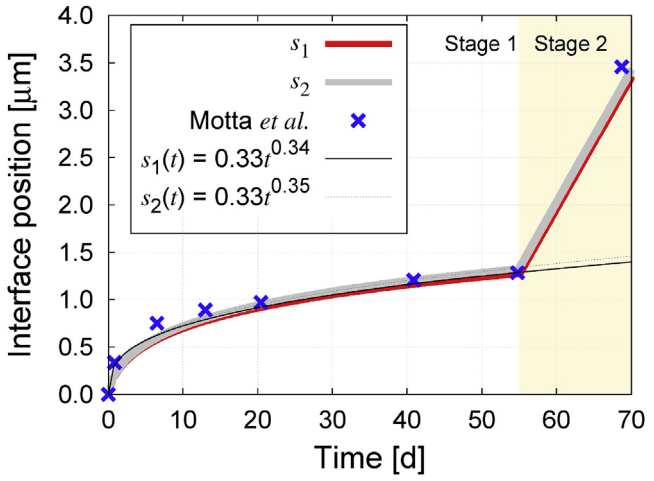

Fig. 7. Evolution of the two interfaces considered in our model, s_1 (oxide scale thickness) and s_2 (ZrO/metal interface). The shaded region to the right indicates the transition from Stage 1 to Stage 2, marked by an abrupt increase in the growth rate of the oxide layer. The solid and dashed black lines are power law fits to the data points during Stage 1. Experimental data from Ref. [102] is shown for comparison.

motion. The shaded areas represent the stoichiometric oxygen concentration, which —as expected— jumps discontinuously at s_1 and s_2. Note that we have expressed oxygen concentrations normalized to the pure Zr atomic density, so that the ZrO_2 layer is characterized by a value of $2\rho_{Zr}$, as dictated by stoichiometry, whereas in the ZrO layer it has a value of one.

We also plot the corresponding oxygen depth profiles for two time instants during Stage 2 (at 60 and 70 days) in Fig. 6. After failure of the oxide scale (at 55 days), oxygen makes its way unimpeded to the ZrO_2/ZrO interface (s_1). For the purposes of oxygen diffusion, this effectively shifts the outer boundary of the clad from $y = 0$ to $y = s_1$, which is now exposed to a fixed oxygen concentration of C_0. After breakaway, then, the oxygen content in the ZrO layer suffers a transient —shown in the figure as a maximum in the concentration curves— driven by such an adjustment.

Tracking the positions of s_1 and s_2 as a function of time allows us to plot the growth of the oxide scale with time, Fig. 7. The value of s_1 represents the thickness of the ZrO_2 layer, while the value $(s_2 - s_1)$ gives the thickness of the ZrO layer (fixed to approximately 65 nm in this study). Both curves display nonlinear behavior up to a thickness of s^* (beginning of Stage 2). Solid and dashed black lines are visual guides representing growth scaling laws ($s(t) = at^b$) with a and b indicated in each case. The main results from these curves are: (i) Up to the breakaway point, the oxide scale grows as $s_1(t) = 0.33t^{0.34}$, where s_1 is expressed in microns when t is in days. For its part, the ZrO/metal interface evolves as $s_2(t) = 0.33t^{0.35}$; (ii) the model has been calibrated such that Stage 2 starts when $s_1 = s^* = 1.27$ μm, which leads to a duration of approximately 55 days for Stage 1; (iii) the oxide scale grows linearly from that point onwards. Notwithstanding the large variability in experimental measurements found in the literature for a given material composition even under nominally equivalent conditions, we include the results from Motta et al. for pure Zr [102] based on which we have chosen the parameters s^* and $t_{1\to2}$.

It is also of interest to study the relative contribution of each of the terms that appear in eq. (10) for oxygen diffusion in the oxide. For this, we switch off each term one at a time and examine the s_1-vs.-t behavior during Stage 1. The results are shown in Fig. 8, which shows three curves, one for each scenario. First, we solve the diffusion equation just with the *Fickian* term. As expected, this gives

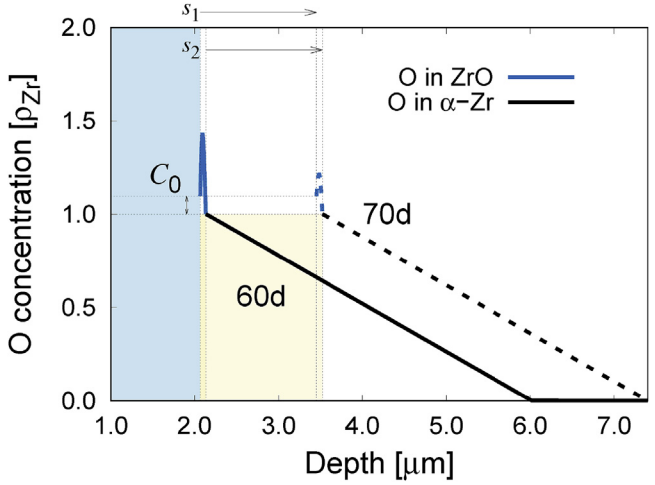

Fig. 6. Depth profile of the total oxygen concentration at two instants during Stage 2. The concentration is expressed as in units of ρ_{Zr}. The shaded areas in the graph represent the thickness of the ZrO_2 and ZrO layers.

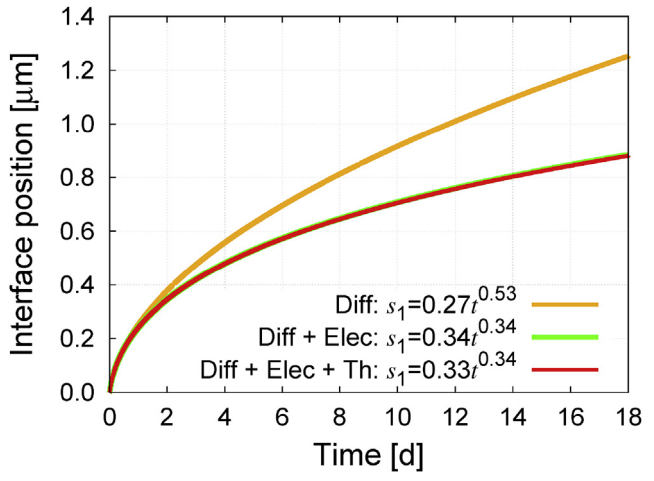

Fig. 8. Analysis of the different contributions to the drift-diffusion equation (eq. (10)) for oxygen buildup in ZrO_2 during Stage 1.

rise to an evolution that is best fit by a $\sim \sqrt{t}$ law. Second, we add electro-migration, which is seen to 'bend' the curve towards a $t^{1/3}$ evolution. Finally, adding thermo-migration results in only variations on the order of 2% in s_1 with respect to the previous case.

3.2. Sensitivity study of relevant parameters

Next, we carry out a sensitivity study of the model by considering its response to variations in key parameter models.

Fig. 9 shows the impact on the growth law for ZrO_2 (in pure Zr) of variations of the oxygen concentration in the environment, C_0 (Fig. 9a), the oxygen diffusivity in the oxide, D_{III} (Fig. 9b), and the charge imbalance at the metal/oxide interface, ρ_0 (Fig. 9c). As the plots show, changes of ±15% in these parameters result in variations of less than 5% in the values of s_1, suggesting that variations in model parameters are 'muffled' by the model itself.

While this analysis cannot be considered an exhaustive uncertainty quantification study, it can nonetheless help us understand the effect of uncertainties in some of the most important parameters entering the model, so that reasonable limits can be set to its applicability.

3.3. Effect of alloy composition

Another important aspect to consider is the impact of alloy composition on the model predictions. Motta et al. have provided an excellent compendium of the qualitative effects of alloy composition on Zr oxidation [102], while Bell et al. have recently discussed the issue using electronic structure arguments [71]. However, gathering complete data sets for different Zr-based alloys is as challenging as it is for pure Zr. Our approach to study chemical composition effects is to choose alloys for which the oxygen diffusivity has been accurately measured (both in the metal and the oxide). As well, we assess the existence of a charge gradient based on the measured time exponents in the experimental literature. Based on these criteria, we have chosen Zircaloy-4 (nominal composition: Zr-1.5Sn-0.2Fe-0.1Cr) [103,104] and Zr-2.5Nb [105] as the subjects of our study. Fig. 10 shows the comparison between the three systems, with the corresponding time exponents given for each case. When plotted in normalized scale, there is virtually no distinction between pure Zr and Zircaloy-4, with both exponents being very similar. Conversely, Zr-2.5Nb displays a quadratic behavior, as established experimentally. From the point of view of our model, this is simply indicative of the role played by electro-migration, which is qualitatively identical for Zr and Zircaloy-4, and nonexistent for Zr-2.5Nb. Their failure thicknesses and transition times are all different and are given in Table 3 along with the value of the oxygen diffusion coefficients and the rest of the fitting parameters.

4. Discussion of results

The results shown in the previous section reveal the potential of our methodology, which uses a three-layer spatio-temporal description of the oxidation process in Zr, to model oxygen corrosion kinetics in nuclear environments. Our approach is based on a *Stefan* interface tracking model to represent the motion of the two interfaces representing the three layers. These layers are tied together via mass conservation boundary conditions, for which drift-diffusion equations must be solved simultaneously.

The spatial dependence in the model is only one-dimensional, along the depth direction, which simplifies the numerical treatment of the equation system. Although such a simplification disregards the formation of the oxide from a grain nucleation and growth process, which is known to be the operating mechanism in

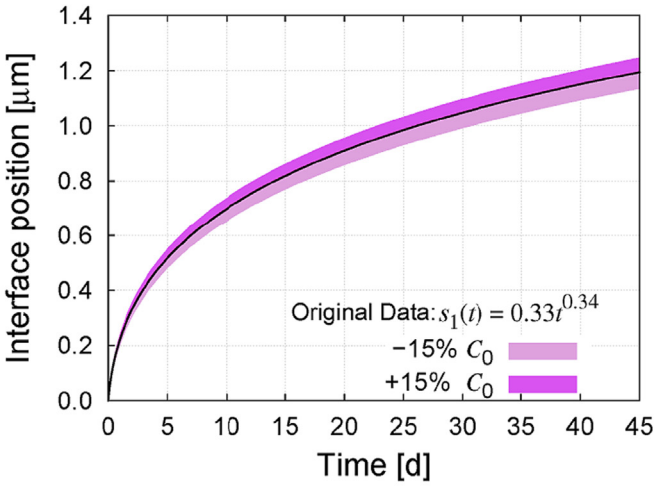

(a) Variation of s_1 with a ±15% in the value of C_0.

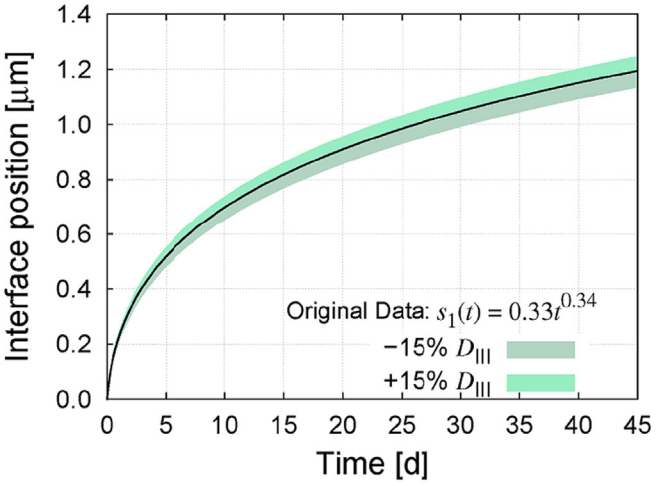

(b) Variation of s_1 with a ±15% in the value of D_{III}.

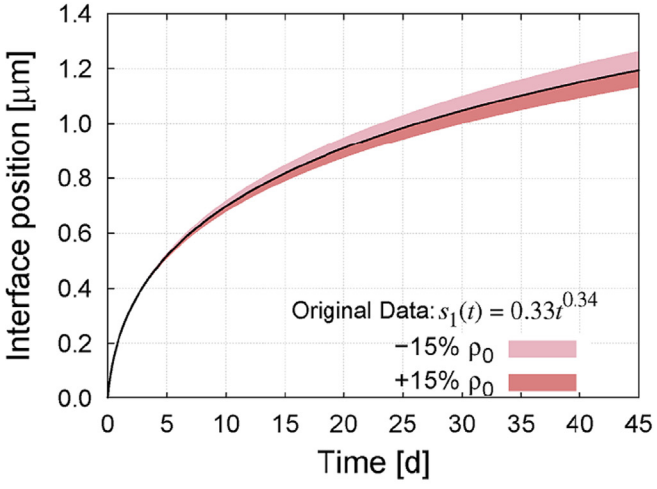

(c) Variation of s_1 with a ±15% in the value of ρ_0.

Fig. 9. Sensitivity of the growth law of ZrO_2 (in pure Zr) to ±15% variations of key model parameters.

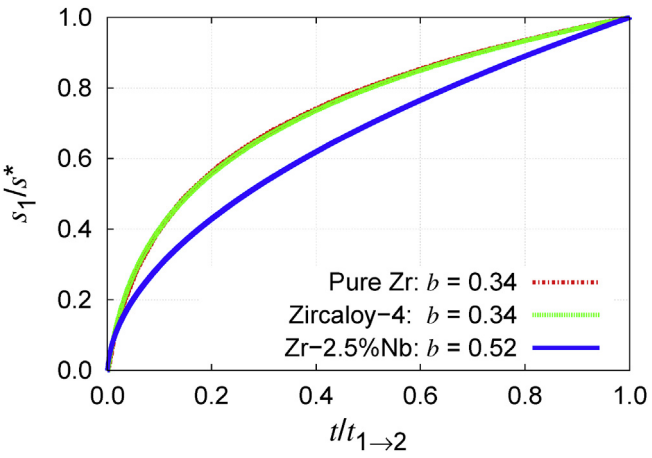

Fig. 10. Evolution laws for the oxide scale thickness for pure Zr, Zircaloy-4, and Zr-2.5Nb. To facilitate the comparison, the graph has been rescaled to the failure thickness s^* (abscissa) and failure time $t_{1\to 2}$ (ordinate) in each case. The time exponent b in the expression $s_1(t) = at^b$ is given as a reference.

Zr clad corrosion, the model contains features that are indirectly associated with a polycrystalline microstructure, such as the formation of a substoichiometric (tetragonal) oxide phase near the interface and fragmentation after a certain time. Another, perhaps less limiting, simplification is that O and Zr are the only chemical species considered here, when it is well known that hydrogen and water chemistry do have a strong impact on the oxidation kinetics, as does alloy composition in Zr alloys.

This capability to capture a multilayer representation of the oxidation process is one of the main features of the model. The literature is increasingly indicative of a situation in which ZrO is seen to form in out-of-pile (autoclave or corrosion loop) conditions, while under in-pile conditions this phase has not been yet detected. We have already presented a version of our model that captures the distinct formation of the tetragonal oxide layer behind the main monoclinic phase [60]. The reasons behind the suppression of the ZrO region in in-pile conditions are not yet clear, but for the moment we limit our model to out-of-pile conditions and leave other aspects of irradiation for future studies. As well, the third line compound, $ZrO_{1/2}$, that has both been predicted by DFT calculations and seen in experiments is not considered in our model, as, in our mind, the difficulties of formulating a four-layer model outweigh the benefits of including this extra compound.

The inherent complexity of the oxidation process requires that models use a combination of *first-principles* and (semi)phenomenological elements in their formulation. Similarly, the model parameters originate both from experiments (typically several decades old), and very recent electronic structure calculations. One must always exercise care when mixing both sources of data, as they are often not exchangeable. Often times, however, using calculations is the only way to obtain critical model parameters and material constants, as we have shown in this work.

Two key parameters merit a more detailed discussion. Our model is designed in principle for pure Zr and Zircaloy, for which detailed experimental information exists. For example, pure Zr is known to transition into Stage 2 oxidation at a critical scale thickness of 1-to-2 μm, while Zircaloy-4 is seen to fail around 2.5 μm. In both cases, Stage 1 is characterized by $t^{1/3}$ kinetics. We have used the parameters C_0 and ρ_0 to recover such behavior. Evidently, more than one combination of values for these two parameters can yield the desired results. We recognize this and cautiously note that the values employed here are not definitive, other than we have not let them fluctuate uncontrollably and have made sure that they stay within reasonable experimental limits. The main point is that, although electro-migration −induced by charge accumulation in a localized region near the oxide interface− can bend the standard diffusive curves $\sim t^{1/2}$ in both directions, only a suitable choice of parameters can furnish the experimentally-observed $t^{1/3}$ behavior. This has been known in the community for some time [67,106], and here we present a modeling effort showcasing precisely how to achieve that.

In terms of the numerics, the model is solved using an explicit second-order finite difference discretization, a very standard method of solving partial differential equations numerically. As it relates to the present calculations, the main difficulties were the timescale used, which is set on the one hand by the material constants employed (e.g. diffusivities, and dielectric constants), and on the other by numerical stability criteria that set limits on the value of the time increments that can be used. Because the the relationship between δt and δy (cf. Sec. 2.7) is material constant dependent, achieving time synchronicity across the different zones is not entirely trivial and an extra constraint must be added to the time step to ensure that the interfaces evolve on the same timescale.

Finally, our model does not explicitly capture irradiation effects. Multiple studies have shown that Stage 1 is only slightly affected by irradiation, with the major effect shown on Stage 2 kinetics [53,107]. However, newer data suggests that higher dose rates significantly accelerate oxidation during the early stages of corrosion [108]. As mentioned above, a model incorporating these effects is underway and will published in the future. Our emphasis so far has been on capturing the cubic growth kinetics for Stage 1 oxidation and develop a mechanical failure criterion that provides a physically based transition to Stage 2 kinetics. On a qualitative level, both of these goals have been attained, although much work remains to be done to fully understand the peculiarities of Zr oxidation in nuclear environments.

5. Conclusions

We end this paper with a list of the most important conclusions:

- We have developed a one-dimensional numerical model of oxide scale formation and growth in zirconium under nuclear reactor operating conditions. The model tracks the motion of interfaces governed by oxygen diffusion, which includes concentration driven transport, thermo-migration, and electro-migration.

Table 3
Comparison of parameters for Zr, Zirc-4, and Zr-2.5Nb. The parameters for pure Zr are directly taken from Table 1. Data for Zircaloy-4 is taken from Refs. [103,104], while the parameters for Zr-2.5Nb are from Zhang et al. [105].

	s^* [μm]	$t_{1\to 2}$ [days]	D_{I}^0 [$m^2 s^{-1}$]	U_{I} [eV]	D_{III}^0 [$m^2 \cdot s^{-1}$]	U_{III} [eV]	C_0 [ρ_{Zr}]	ρ_0 [$C \cdot m^{-2}$]
Zr	1.27	40	6.61×10^{-6}	1.9	9.00×10^{-8}	1.24	0.36	662.0
Zirc-4	2.47	149	3.92×10^{-4}	2.2	2.76×10^{-6}	1.5	0.52	156.0
Zr-2.5Nb	2.41	112	1.72×10^{-5}	1.9	1.72×10^{-5}	1.9	142.22	0.0

- The model includes the formation of three layers: ZrO_2 (outermost), ZrO (middle), and metallic Zr suboxides and solid-solutions (innermost). As well, certain aspects of the model reflect the existence of a substoichiometric tetragonal Zr near the ZrO_2/ZrO oxide interface.
- A mechanical failure criterion based on oxide fragmentation and Pilling-Bedworth stresses has been derived to predict the transition from Stage 1 to Stage 2.
- The model is parameterized with both experimental and computational data, and it captures a full temperature dependence across the Zr clad.
- Our results show that cubic growth behavior can be predicted when electro-migration is considered, and a suitable choice of parameters is adopted. These parameters are fitted to reasonable values that yield the desired behavior.
- The sharp transition to breakaway growth in Stage 2 after oxide scale fragmentation occurs as a consequence of the accumulation of compressive stresses in the oxide/metal interface.
- A preliminary sensitivity analysis has been conducted, showing that changes of ±15% in key model parameters results in variations of less than 5% in the time-dependentkinetics of the oxide layer.

Acknowledgments

This research was supported by the Consortium for Advanced Simulation of Light Water Reactors (CASL), an Energy Innovation Hub for Modeling and Simulation of Nuclear Reactors under U.S. Department of Energy Contract No. DE-AC05-00OR22725. Helpful discussions with A. Couet, A. Motta, B. D. Wirth, and A. Van der Ven are acknowledged.

Appendix A. Analytical justification for an exponentially-decaying charge density

The charge density in the vicinity of a chemical reaction site can be safely assumed to be maximum at the reaction site and to gradually decrease towards zero with distance from it (in the limit of an electro-neutral medium). Several works have suggested that such decrease can take the form of an exponential decay [109,110]. Here, we derive an expression for the charge density that follows an exponential decay from simple kinetic considerations.

The accumulation of charge near a moving corrosion reaction front results from an imbalance between positively and negatively charged species. Assuming first-order kinetics, this excess charge is consumed at a rate given by:

$$\frac{d\rho}{dt} = -\alpha\rho \tag{A.1}$$

where ρ is the charge density and α is a constant. As well, if the corrosion front is moving with a velocity $v = dx/dt$, the time change of the charge density can also be expressed as:

$$\frac{d\rho}{dt} = \frac{d\rho}{dx}\frac{dx}{dt} = v\frac{d\rho}{dx} \tag{A.2}$$

Combining eqs. (A.1) and (A.2) leads to:

$$\frac{d\rho}{dx} = -\frac{\alpha}{v}\rho \tag{A.3}$$

Although the velocity of the oxidation front changes with time, this change rate can be considered much slower than the local charge density variation. Consequently, the advancing reaction front is assumed to advance at a constant velocity v such that integration of eq. (A.3) results in:

$$\rho(x) = \rho_0 \exp\left(-\frac{\alpha}{v}x\right) \tag{A.4}$$

where ρ_0 is the charge density at the moving interface, and the ratio $\frac{\alpha}{v}$ is denoted by the constant λ in Section 2.3.

Appendix B. Stability criterion

The Neumann stability criterion for linear differential equations with periodic boundary conditions allows us to expand the solution in a finite Fourier series. Each Fourier mode, defined by its wave number ω, is tracked in time assuming a simple separable solution of the form[8]:

$$c_J^I = b(t_I)e^{iJ\omega\delta y}$$

such that eq. (24) transforms into:

$$b^{I+1}\exp[iJ\omega\delta y] = (a_1+a_2+a_3+a_4)b^I\exp[i(J+1)\omega\delta y] + (1-2a_1+a_5)b^I\exp[iJ\omega\delta y] + \\ +(a_1+a_2+a_3+a_4)b^I\exp[i(J-1)\omega\delta y] \tag{B.1}$$

Von Neumann's analysis applies to periodic systems where the coefficients a_1, a_2, a_3, a_4, and a_5 are constant in time and space. Strictly speaking, this is not satisfied in cases with varying temperature gradients, but it can generally be assumed to hold when the coefficients vary slowly. Operating with the above equation:

$$b^{I+1}\exp\left[iJ\omega\delta y\right] = b^I\exp\left[iJ\omega\delta y\right]\left[(a_1+a_2+a_3+a_4)\exp\left[i\omega\delta y\right] + (1-2a_1+a_5) + \right. \\ \left. +(a_1+a_2+a_3+a_4)b^I\exp\left[-i\omega\delta y\right]\right] \tag{B.2}$$

[8] Note that in this appendix we use I and J as the temporal and spatial indices, to distinguish them from the complex variable i.

which can then simplified to:

$$\xi = \frac{b^{l+1}}{b^l} = 1 - 2a_1 + a_5 + (a_1 + a_2 + a_3 + a_4)\left(e^{i\omega\delta y} + e^{-i\omega\delta y}\right) \tag{B.3}$$

Noting that:

$$e^{\pm i\omega\delta y} = \cos(\omega\delta y) \pm i\sin(\omega\delta y),$$

we can rewrite (B.3) as:

$$\xi = \frac{b^{l+1}}{b^l} = 1 - 2a_1 + a_5 + 2(a_1 + a_2 + a_3 + a_4)\cos(\omega\delta y) \tag{B.4}$$

The Neumann stability criterion is defined as:

$$\xi^2 \leqslant 1 \tag{B.5}$$

$$\xi^2 = (1 - 2a_1 + a_5 + 2(a_1 + a_2 + a_3 + a_4)\cos(\omega\delta y))^2 \tag{B.6}$$

We consider the two extrema of trigonometric functions $\omega\delta y = 0$ and $\omega\delta y = \frac{\pi}{2}$. In the former case, the stability condition is simply:

$$a_5 \leqslant 2a_1$$

whereas for $\omega\delta y = \pi/2$ we have:

$$a_5 \geqslant 2(a_2 + a_3 + a_4)$$

The combination of both conditions results in:

$$a_2 + a_3 + a_4 \leqslant 1 \tag{B.7}$$

Substituting for the expressions of each coefficient from Section 2.7 and operating, we arrive at:

$$\delta t \leqslant \frac{2kT}{D\left(\frac{U}{T}\frac{\partial T}{\partial y} + \frac{q\lambda(\rho(y)-\rho_0)}{\varepsilon}\right)}\delta y \tag{B.8}$$

which sets limits on the admissible values for δt and δy.

References

[1] J.C. Scully, The Fundamentals of Corrosion, vol. 2, 1978.
[2] N. North, I.D. MacLeod, C. Pearson, Corrosion of Metals, Butterworth-Heinemann, 1987.
[3] D.J. Young, High Temperature Oxidation and Corrosion of Metals, vol. 1, Elsevier, 2008.
[4] P. Jacques, F. Lefebvre, C. Lemaignan, Deformation–corrosion interactions for zr alloys during i-scc crack initiation: part i: chemical contributions, J. Nucl. Mater. 264 (3) (1999) 239–248.
[5] G.P. Sabol, G.D. Moan, Zirconium in the Nuclear Industry: Twelfth International Symposium, ASTM, 2000.
[6] D. Feron, Nuclear Corrosion Science and Engineering, first ed., vol. 10, Woodhead Publishing, 2012.
[7] F. Cattant, D. Crusset, D. FÃ©ron, Corrosion issues in nuclear industry today, Mater. Today 11 (10) (2008) 32–37. https://doi.org/10.1016/S1369-7021(08)70205-0. http://www.sciencedirect.com/science/article/pii/S1369702108702050.
[8] T. Allen, R. Konings, A. Motta, 5.03 corrosion of zirconium alloys, Comprehensive nuclear materials (2012) 49–68.
[9] E. Hillner, Corrosion of zirconium-base alloys?an overview, in: Zirconium in the Nuclear Industry, ASTM International, 1977.
[10] A. Zaimovskii, Zirconium alloys in nuclear power, Atom. Energy 45 (6) (1978) 1165–1168.
[11] B. Cox, Some thoughts on the mechanisms of in-reactor corrosion of zirconium alloys, J. Nucl. Mater. 336 (2) (2005) 331–368.
[12] R.A. Causey, D.F. Cowgill, R.H. Nilson, Review of the Oxidation Rate of Zirconium Alloys, Tech. Rep, Sandia National Laboratories, 2005.
[13] A.T. Motta, A. Yilmazbayhan, M.J.G. da Silva, R.J. Comstock, G.S. Was, J.T. Busby, E. Gartner, Q. Peng, Y.H. Jeong, J.Y. Park, Zirconium alloys for supercritical water reactor applications: challenges and possibilities, J. Nucl. Mater. 371 (1) (2007) 61–75.
[14] P. Bossis, D. Pecheur, K. Hanifi, J. Thomazet, M. Blat, Comparison of the high burn-up corrosion on m5 and low tin zircaloy-4, in: 14th International Symposium on Zirconium in the Nuclear Industry, vol. 3, 2006, pp. 494–525.
[15] C.M. Eucken, P.T. Finden, S. Trapp-Pritsching, H.G. Weidinger, Influence of chemical composition on uniform corrosion of zirconium-base alloys in autoclave tests, in: Zirconium in the Nuclear Industry: Eighth International Symposium, ASTM International, 1989.
[16] R.A. Graham, J.P. Tosdale, P.T. Finden, Influence of chemical composition and manufacturing variables on autoclave corrosion of the zircaloys, in: Zirconium in the Nuclear Industry: Eighth International Symposium, ASTM International, 1989.
[17] Z. Bangxin, L. Qiang, L. Wenqing, Y. Meiyi, C. Yuliang, The effects of water chemistry and composition on the microstructure evolution of oxide films on zirconium alloys during autoclave tests, Rare Metal Mater. Eng. 35 (7) (2006) 1009.
[18] P. Billot, A. Giordano, Comparison of zircaloy corrosion models from the evaluation of in-reactor and out-of-pile loop performance, in: Zirconium in the Nuclear Industry: Ninth International Symposium, ASTM International, 1991.
[19] E. Hillner, D. Franklin, J. Smee, Long-term corrosion of zircaloy before and after irradiation, J. Nucl. Mater. 278 (2) (2000) 334–345.
[20] X. Iltis, F. Lefebvre, C. Lemaignan, Microstructural study of oxide layers formed on zircaloy-4 in autoclave and in reactor part i: impact of irradiation on the microstructure of the zirconia layer, J. Nucl. Mater. 224 (2) (1995) 109–120.
[21] A. Yilmazbayhan, A.T. Motta, R.J. Comstock, G.P. Sabol, B. Lai, Z. Cai, Structure of zirconium alloy oxides formed in pure water studied with synchrotron radiation and optical microscopy: relation to corrosion rate, J. Nucl. Mater. 324 (1) (2004) 6–22.
[22] A. Denis, E. Moyano, E.A. Garcia, Model to simulate high temperature oxidation kinetics of zircaloy-4: parabolic and linear behaviour, J. Nucl. Mater. 110 (1) (1982) 11–19.
[23] J.A. Nesbitt, Numerical modeling of high-temperature corrosion processes, Oxid. Metals 44 (1) (1995) 309–338, https://doi.org/10.1007/BF01046731. https://doi.org/10.1007/BF01046731.
[24] B. Cheng, P. Gilmore, H. Klepfer, Pwr zircaloy fuel cladding corrosion performance, mechanisms, and modeling, in: Zirconium in the Nuclear Industry: Eleventh International Symposium, ASTM International, 1996.
[25] T. Arima, T. Masuzumi, H. Furuya, K. Idemitsu, Y. Inagaki, The oxidation kinetics and the structure of the oxide film on zircaloy before and after the kinetic transition, J. Nucl. Mater. 294 (1?2) (2001) 148–153, 10th Int. Symp. on Thermodynamics of Nuclear Materials, https://doi.org/10.1016/S0022-3115(01)00453-6, http://www.sciencedirect.com/science/article/pii/S0022311501004536.
[26] V. Busser, J. Desquines, S. Fouquet, M.C. Baietto, J.P. Mardon, Modelling of corrosion induced stresses during zircaloy-4 oxidation in air, in: Materials Science Forum, vol. 595, Trans Tech Publ, 2008, pp. 419–427.
[27] P. Platt, E. Polatidis, P. Frankel, M. Klaus, M. Gass, R. Howells, M. Preuss, A study into stress relaxation in oxides formed on zirconium alloys, J. Nucl. Mater. 456 (2015) 415–425. https://doi.org/10.1016/j.jnucmat.2014.09.072. http://www.sciencedirect.com/science/article/pii/S0022311514006722.
[28] Review of theoretical conceptions on regimes of oxidation and hydrogen pickup in Zr-alloys.
[29] M. Steinbrück, J. Birchley, A. Goryachev, M. Grosse, T. Haste, Z. Hozer, A. Kisselev, V. Nalivaev, V. Semishkin, L. Sepold, et al., Status of studies on high-temperature oxidation and quench behaviour of zircaloy-4 and e110 cladding alloys, ERMSAR, Nesseber, Bulgaria, 2008. Session S 2.
[30] M. Lindgren, I. Panas, On the fate of hydrogen during zirconium oxidation by water: effect of oxygen dissolution in [small alpha]-zr, RSC Adv. 4 (2014) 11050–11058, https://doi.org/10.1039/C4RA00020J. https://doi.org/10.1039/C4RA00020J.
[31] F. Garzarolli, H. Seidel, R. Tricot, J. Gros, Oxide growth mechanism on zirconium alloys, in: Zirconium in the Nuclear Industry: Ninth International Symposium, ASTM International, 1991.
[32] L. Zhang, D.D. Macdonald, E. Sikora, J. Sikora, On the kinetics of growth of anodic oxide films, J. Electrochem. Soc. 145 (3) (1998) 898–905, https://doi.org/10.1149/1.1838364.
[33] G.H.M. Birks, N.,F.S. Pettit, Introduction to the High-temperature Oxidation of Metals, Cambridge University Press, New York, 2006.
[34] A. Saillard, Modeling and Simulation of Stress-induced Non-uniform Oxide Scale Growth during High-temperature Oxidation of Metallic Alloys, Ph.D. thesis, Georgia Institute of Technology, 5 2010.
[35] A. Almarshad, A. Klein, A model for waterside oxidation of zircaloy fuel cladding in pressurized water reactors, J. Nucl. Mater. 183 (3) (1991) 186–194. https://doi.org/10.1016/0022-3115(91)90487-R. http://www.sciencedirect.com/science/article/pii/002231159190487R.
[36] J. Belle, M. Mallett, Kinetics of the high temperature oxidation of zirconium, J. Electrochem. Soc. 101 (7) (1954) 339–342.
[37] E. Gulbransen, K. Andrew, Oxidation of zircaloy-2 and -3a at 300 to 850 c, Trans. Met. Soc. AIME Vol: 212.
[38] H.A. Porte, J.G. Schnizlein, R.C. Vogel, D.F. Fischer, Oxidation of Zirconium and Zirconium Alloys, vol. 107, 1960, pp. 506–515, https://doi.org/10.1149/1.2427733 (6).
[39] P. Gondi, G.F. Missigolli, Electron microscope observations on the oxidation of zirconium. a contribution to the cubic kinetic theory, Il Nuovo Cimento

XLVIII B (2) (1967) 223–236.
[40] P. Tejland, H.-O. Andrén, Origin and effect of lateral cracks in oxide scales formed on zirconium alloys, J. Nucl. Mater. 430 (1) (2012) 64–71.
[41] J.P. Abriata, J. Garcés, The o-zr (oxygen-xirconium) system, Bulletin of Alloy Phase Diagrams 7 (2) (1986) 116–124.
[42] E.G. Rauh, S.P. Garg, The zro_{2-x} (cubic)-zro_{2-x} (cubic + tetragonal) phase boundary, J. Am. Ceram. Soc. 63 (1980) 239–240.
[43] E. Gebhardt, H.D. Seghezzi, W. Durrschnabel, Research on the system zirconium-oxide, J. Nucl. Mater. 4 (1961) 255–268.
[44] B. Puchala, A. Van der Ven, Thermodynamics of the zr-o system from first-principles calculations, Phys. Rev. B 88 (2013), 094108.
[45] Y. Dong, A.T. Motta, E.A. Marquis, Atom probe tomography study of alloying element distributions in zr alloys and their oxides, J. Nucl. Mater. 442 (1) (2013) 270–281.
[46] R.J. Nicholls, N. Ni, S. Lozano-Perez, A. London, D.W. McComb, P.D. Nellist, C.R. Grovenor, C.J. Pickard, J.R. Yates, Crystal structure of the zro phase at zirconium/zirconium oxide interfaces, Adv. Eng. Mater. 17 (2) (2015) 211–215.
[47] K.J. Annand, I. MacLaren, M. Gass, Utilising dual eels to probe the nanoscale mechanisms of the corrosion of zircaloy-4 in 350°c pressurised water, J. Nucl. Mater. 465 (2015) 390–399. https://doi.org/10.1016/j.jnucmat.2015.06.022. http://www.sciencedirect.com/science/article/pii/S0022311515300477.
[48] Corrosion of Zirconium Alloys in Nuclear Power Plants, Tech. Rep. IAEA-tecdoc-684, International Atomic Energy Agency, 1993.
[49] R.C. Garvie, R.H. Hannik, R.T. Pascoe, Ceramic steel? Nature 258 (1975) 703–704.
[50] J. Godlewski, How the Tetragonal Zirconia Is Stabilized in the Oxide Scale that Is Formed on a Zirconium alloy Corroded at 400° C in Steam, ASTM International, West Conshohocken, PA, 1994, pp. 663–683.
[51] R.C. Garvie, Ceramic steel? J. Phys. Chem. 69 (1965) 1238–1243.
[52] M.W. Pitcher, S.V. Ushakov, A. Navrotsky, B.F. Woodfield, G. Li, J. Boerio-Goates, B.M. Tissue, Energy crossovers in nanocrystalline zirconia, J. Am. Ceram. Soc. 88 (1) (2005) 160–167, https://doi.org/10.1111/j.1551-2916.2004.00031.x. https://doi.org/10.1111/j.1551-2916.2004.00031.x.
[53] A.T. Motta, A. Couet, R.J. Comstock, Corrosion of zirconium alloys used for nuclear fuel cladding, Annu. Rev. Mater. Res. 45 (1) (2015) 311–343.
[54] A. Garner, A. Gholinia, P. Frankel, M. Gass, I. MacLaren, M. Preuss, The microstructure and microtexture of zirconium oxide films studied by transmission electron backscatter diffraction and automated crystal orientation mapping with transmission electron microscopy, Acta Mater. 80 (2014) 159–171. https://doi.org/10.1016/j.actamat.2014.07.062. http://www.sciencedirect.com/science/article/pii/S1359645414005801.
[55] G.S. Frankel, Fundamentals of corrosion kinetics, in: A.E. Hughes, J.M. Mol, M.L. Zheludkevich, R.G. Buchheit (Eds.), Active Protective Coatings: New-generation Coatings for Metals, vol. 233, Springer Series in Materials Science, 2016. Ch. 2.
[56] H. Steiner, J. Konys, Stresses in Oxidized Claddings and Mechanical Stability of Oxide Scales, Tech. Rep. FZKA 7191, Forschungszentrum Karlsruhe, 2006.
[57] J. Chevalier, L. Gremillard, A.V. Virkar, D.R. Clarke, The tetragonal-monoclinic transformation in zirconia: lessons learned and future trends, J. Am. Ceram. Soc. 92 (9) (2009) 1901–1920.
[58] E.D. Whitney, Kinetics and mechanism of the transition of metastable tetragonal to monoclinic zirconia, Trans. Faraday Soc. 61 (1965) 1991–2000.
[59] The reaction of oxygen and zirconium, Thermochim. Acta 84 (1985) 357–365.
[60] A. Aryanfar, J. Thomas, A. Van der Ven, D. Xu, M. Youssef, J. Yang, B. Yildiz, J. Marian, Integrated computational modeling of water side corrosion in zirconium metal clad under nominal lwr operating conditions, JOM (J. Occup. Med.) 68 (11) (2016) 2900–2911.
[61] Rubinshteĭ, The Stefan Problem.
[62] J. Cannon, M. Primicerio, Remarks on the one-phase stefan problem for the heat equation with the flux prescribed on the fixed boundary, J. Math. Anal. Appl. 35 (2) (1971) 361–373.
[63] A. Crowley, On the weak solution of moving boundary problems, IMA J. Appl. Math. 24 (1) (1979) 43–57.
[64] K. Michel, V. Ozolins, Theory of mass transport in sodium alanate, J. Mater. Chem. 2 (2014) 4438.
[65] G.D. Rieck, H.A.C.M. Bruning, Thermal diffusion of oxygen and nitrogen in zirconium, Nature 190 (1961) 1181–1182.
[66] T.-W. Chiang, A. Chernatynskiy, M.J. Noordhoek, S.B. Sinnott, S.R. Phillpot, Anisotropy in oxidation of zirconium surfaces from density functional theory calculations, Comput. Mater. Sci. 98 (2015) 112–116. https://doi.org/10.1016/j.commatsci.2014.10.052. http://www.sciencedirect.com/science/article/pii/S0927025614007502.
[67] A. Couet, A.T. Motta, A. Ambard, The coupled current charge compensation model for zirconium alloy fuel cladding oxidation: I. parabolic oxidation of zirconium alloys, Corrosion Sci. 100 (2015) 73–84. http://doi.org/10.1016/j.corsci.2015.07.003. http://www.sciencedirect.com/science/article/pii/S0010938X15300019.
[68] G. Eloff, C. Greyling, P. Viljoen, The role of space charge in the oxidation of zircaloy-4 between 350 and 450Â°c in air, J. Nucl. Mater. 199 (3) (1993) 285–288. https://doi.org/10.1016/0022-3115(93)90149-S. http://www.sciencedirect.com/science/article/pii/002231159390149S.
[69] H.-J. Beie, A. Mitwalsky, F. Garzarolli, H. Ruhmann, H.-J. Sell, Examinations of the corrosion mechanism of zirconium alloys, in: Zirconium in the Nuclear Industry: Tenth International Symposium, ASTM International, 1994.
[70] B. Bell, S. Murphy, P. Burr, R. Comstock, J. Partezana, R. Grimes, M. Wenman, The influence of alloying elements on the corrosion of zr alloys, Corrosion Sci. 105 (2016) 36–43. https://doi.org/10.1016/j.corsci.2015.12.022. http://www.sciencedirect.com/science/article/pii/S0010938X15302006.
[71] B. Bell, S. Murphy, R. Grimes, M. Wenman, The effect of nb on the corrosion and hydrogen pick-up of zr alloys, Acta Mater. 132 (2017) 425–431. https://doi.org/10.1016/j.actamat.2017.04.063. http://www.sciencedirect.com/science/article/pii/S1359645417303579.
[72] M. Mamivand, M.A. Zaeem, H.E. Kadiri, L.-Q. Chen, Phase field modeling of the tetragonal-to-monoclinic phase transformation in zirconia, Acta Mater. 61 (14) (2013) 5223–5235.
[73] P. Platt, P. Frankel, M. Gass, R. Howells, M. Preuss, Finite element analysis of the tetragonal to monoclinic phase transformation during oxidation of zirconium alloys, J. Nucl. Mater. 454 (1) (2014) 290–297. https://doi.org/10.1016/j.jnucmat.2014.08.020. http://www.sciencedirect.com/science/article/pii/S0022311514005480.
[74] H. Evans, R. Lobb, Conditions for the initiation of oxide-scale cracking and spallation, Corrosion Sci. 24 (3) (1984) 209–222.
[75] J. Armitt, R. Holmes, M. Manning, D. Meadowcroft, E. Metcalfe, Spalling of Steam-grown Oxide from Superheater and Reheater Tube Steels. Technical Planning Study 76-655, final report, Tech. rep, Central Electricity Research Labs., Leatherhead (UK), 1978.
[76] N. Tang, A. Plumtree, Cavity nucleation in creep, Scripta Metallurgica 18 (10) (1984) 1045–1049.
[77] J. Wanklyn, C. Britton, D. Silvester, N. Wilkins, Influence of environment on the corrosion of zirconium and its alloys in high-temperature steam, J. Electrochem. Soc. 110 (8) (1963) 856–866.
[78] What is wrong with current models for in-reactor corrosion, in: Fundamental Aspects of Corrosion on Zirconium Base Alloys in Water Reactor Environments.
[79] B. Cox, Some thoughts on the mechanisms of in-reactor corrosion of zirconium alloys, J. Nucl. Mater. 336 (2?3) (2005) 331–368. https://doi.org/10.1016/j.jnucmat.2004.09.029. http://www.sciencedirect.com/science/article/pii/S002231150400875X.
[80] J.P. Pemsler, Diffusion of oxygen in zirconium and its relation to oxidation and corrosion, J. Electrochem. Soc. 105 (6) (1958) 315–322, https://doi.org/10.1149/1.2428837 arXiv: http://jes.ecsdl.org/content/105/6/315.full.pdf+html http://jes.ecsdl.org/content/105/6/315.abstract.
[81] I. Ritchie, A. Atrens, The diffusion of oxygen in alpha-zirconium, J. Nucl. Mater. 67 (3) (1977) 254–264. https://doi.org/10.1016/0022-3115(77)90097-6. http://www.sciencedirect.com/science/article/pii/0022311577900976.
[82] T. Smith, Diffusion coefficients and anion vacancy concentrations for the zirconium-zirconium dioxide system, J. Electrochem. Soc. 112 (6) (1965) 560–567.
[83] C.O.D. GonzÃ¡lez, E.A. GarcÃa, Determination of the diffusion coefficients of oxygen in zirconium by means of xps, Appl. Surf. Sci. 44 (3) (1990) 211–219. https://doi.org/10.1016/0169-4332(90)90052-2. http://www.sciencedirect.com/science/article/pii/0169433290900522.
[84] A. Madeyski, W. Smeltzer, Oxygen diffusion in monoclinic zirconia, Mater. Res. Bull. 3 (4) (1968) 369–375. https://doi.org/10.1016/0025-5408(68)90008-1. http://www.sciencedirect.com/science/article/pii/0025540868900081.
[85] D.J. Poulton, W.W. Smeltzer, Oxygen diffusion in monoclinic zirconia, J. Electrochem. Soc. 117 (3) (1970) 378–381, https://doi.org/10.1149/1.2407515 arXiv: http://jes.ecsdl.org/content/117/3/378.full.pdf+html http://jes.ecsdl.org/content/117/3/378.abstract.
[86] F.J. Keneshea, D.L. Douglass, The diffusion of oxygen in zirconia as a function of oxygen pressure, Oxid. Metals 3 (1) (1971) 1–14, https://doi.org/10.1007/BF00604736. https://doi.org/10.1007/BF00604736.
[87] B. Cox, J. Pemsler, Diffusion of oxygen in growing zirconia films, J. Nucl. Mater. 28 (1) (1968) 73–78. https://doi.org/10.1016/0022-3115(68)90058-5. http://www.sciencedirect.com/science/article/pii/0022311568900585.
[88] J. Fink, L. Leibowitz, Thermal conductivity of zirconium, J. Nucl. Mater. 226 (1?2) (1995) 44–50. https://doi.org/10.1016/0022-3115(95)00110-7. http://www.sciencedirect.com/science/article/pii/0022311595001107.
[89] P. Klemens, Thermal conductivity of zirconia, Therm. Conduct. 23 (1996) 209–220.
[90] B. Nait-Ali, K. Haberko, H. Vesteghem, J. Absi, D. Smith, Thermal conductivity of highly porous zirconia, J. Eur. Ceram. Soc. 26 (16) (2006) 3567–3574. https://doi.org/10.1016/j.jeurceramsoc.2005.11.011. http://www.sciencedirect.com/science/article/pii/S095522190500943X.
[91] S. Gu, T.J. Lu, D.D. Hass, H.N.G. Wadley, Thermal conductivity of zirconia coatings with zig-zag pore microstructures, Acta Mater 49 (2001) 2539–2547.
[92] J. Chang, Y.-S. Lin, Dielectric property and conduction mechanism of ultra-thin zirconium oxide films, Appl. Phys. Lett. 79 (22) (2001) 3666–3668.
[93] K. Kukli, K. Forsgren, M. Ritala, M. Leskelä, J. Aarik, A. Haårsta, Dielectric properties of zirconium oxide grown by atomic layer deposition from iodide precursor, J. Electrochem. Soc. 148 (12) (2001) F227–F232.
[94] M. Houssa, V. Afanasev, A. Stesmans, M. Heyns, Variation in the fixed charge density of sio x/zro 2 gate dielectric stacks during postdeposition oxidation, Appl. Phys. Lett. 77 (12) (2000) 1885–1887.
[95] N. Maity, R. Maity, R. Thapa, S. Baishya, Study of interface charge densities for zro2 and hfo2 based metal-oxide-semiconductor devices, Adv. Mater. Sci. Eng. 2014 (2014), 497274. https://www.hindawi.com/journals/amse/2014/

497274/.
[96] P. ALDEBERT, J.-P. TRAVERSE, Structure and ionic mobility of zirconia at high temperature, J. Am. Ceram. Soc. 68 (1) (1985) 34–40, https://doi.org/10.1111/j.1151-2916.1985.tb15247.x. https://doi.org/10.1111/j.1151-2916.1985.tb15247.x.
[97] S.-K. Chan, Y. Fang, M. Grimsditch, Z. Li, M.V. Nevitt, W.M. Robertson, E.S. Zouboulis, Temperature dependence of the elastic moduli of monoclinic zirconia, J. Am. Ceram. Soc. 74 (7) (1991) 1742–1744, https://doi.org/10.1111/j.1151-2916.1991.tb07177.x. https://doi.org/10.1111/j.1151-2916.1991.tb07177.x.
[98] E. Yeugo Fogaing, Y. Lorgouilloux, M. Huger, C.P. Gault, Young?s modulus of zirconia at high temperature, J. Mater. Sci. 41 (2006) 7663–7666.
[99] Zirconia - physical and mechanical property comparison of the different types of zirconias. URL http://www.azom.com/article.aspx?ArticleID=133.
[100] T. Mitsuhashi, T. Ikegami, A. Watanabe, S. Matsuda, Thermodynamics of zirconia system with a possibility of intelligent characters, Proc. Int. Conf. Intell. Mater. 1 (1992) 155–158.
[101] P. Billot, B. Cox, K. Ishigure, A. Johnson, C. Lemaignan, A. Nechaev, N. Petrik, E. Reznichenko, I. Ritchi, G. Sukhanov, Corrosion of zirconium alloys in nuclear power plants, in: TECDOC-684, International Atomic Energy Agency (IAEA), 1993.
[102] A. Motta, M.G. da Silva, A. Yilmazbayhan, R. Comstock, Z. Cai, B. Lai, Microstructural characterization of oxides formed on model zr alloys using synchrotron radiation, in: Zirconium in the Nuclear Industry: 15th International Symposium, ASTM International, 2009.
[103] R. Piotrkowski, A. Denis, J. Kovacs, E. Garcia, Materials interactions during high temperature transients: discussion about the use of the kinetic rate constants in zircaloy oxidation, J. Nucl. Mater. 202 (3) (1993) 252–265.
[104] E. Garcia, G. Béranger, Diffusion model for the oxidation of zircaloy-4 at 400 c in steam. the influence of metallurgical structure (precipitates and grain size), J. Nucl. Mater. 273 (2) (1999) 221–227.
[105] C. Zhang, P.R. Norton, The dissolution of oxide on α -zr (1% nb) and β -zr (20% nb) alloys, J. Nucl. Mater. 300 (1) (2002) 7–14.
[106] A. Couet, A.T. Motta, A. Ambard, D. Livigni, In-situ electrochemical impedance spectroscopy measurements of zirconium alloy oxide conductivity: relationship to hydrogen pickup, Corrosion Sci. 119 (2017) 1–13. https://doi.org/10.1016/j.corsci.2016.12.008. http://www.sciencedirect.com/science/article/pii/S0010938X16308204.
[107] C. Allison, G. Berna, R. Chambers, E. Coryell, K. Davis, D. Hagrman, D. Hagrman, N. Hampton, J. Hohorst, R. Mason, et al., Scdap/relap5/mod3. 1 Code Manual Volume Iv: Matpro–a Library of Materials Properties for Light-water-reactor Accident Analysis, DT Hagrman, NUREG/CR-6150, EGG-2720 4, 1993, 4–234.
[108] P. Wang, G.S. Was, Experimental validation capabilities at um - zr corrosion and hydrogen pick-up. Presentation at the CASL-FMC All-hands Meeting, 2017.
[109] S. Saraf, M. Markovich, A. Rothschild, Defect chemistry of *Pn* junctions in complex oxides, Phys. Rev. B 82 (2010) 245208, https://doi.org/10.1103/PhysRevB.82.245208. https://link.aps.org/doi/10.1103/PhysRevB.82.245208.
[110] A.-R. Hassan, A. El-Azab, M. Manuel, Electrochemical effects of isolated voids in uranium dioxide, J. Phys. Chem. Solid. 75 (4) (2014) 550–557. https://doi.org/10.1016/j.jpcs.2013.12.017. http://www.sciencedirect.com/science/article/pii/S0022369713004150.